ENGINEERING TRANSACTIONS • *Engng. Trans.* • **58**, 1–2, 15–74, 2010
Polish Academy of Sciences • Institute of Fundamental Technological Research

THE THERMODYNAMICAL THEORY OF ELASTO-VISCOPLASTICITY FOR DESCRIPTION OF NANOCRYSTALLINE METALS

P. P e r z y n a

Institute of Fundamental Technological Research
Polish Academy of Sciences
Pawińskiego 5B, 02-106 Warszawa, Poland

The main objective of the present paper is the development of thermodynamical elasto-viscoplastic constitutive model describing the behaviour of nanocrystalline metals. Only *fcc*, *bcc* and *hcp* metals will be covered in this description, because they are the classes of metals for which systematic experimental observation data sets are available. Investigation of the deformation mechanisms is important for understanding, controlling and optimizing of the mechanical properties of nanocrystalline metals. Strengthening with grain size refinement in metals and alloys, with an average grain size of 100 nm or larger, has been well characterized by the Hall-Petch (H-P) relationship, where dislocation pile-up against grain boundaries, along with other transgranular dislocations mechanisms, are the dominant strength-controlling processes. When the average, and entire range of grain sizes is reduced to less than 100 nm, the dislocation operation becomes increasingly more difficult and grain boundary-mediated processes become increasingly more important. The principal short-range barrier, the Peierls-Nabarro stress, is important for ultrafine crystalline *bcc* metals, whereas in ultrafine crystalline *fcc* and *hcp* metals, forest dislocations are the primary short-range barriers at lower temperatures. Experimental observations have shown that nanosized grains rotate during plastic deformation and can coalesce along directions of shear, creating larger paths for dislocation movement.

The model is developed within the thermodynamic framework of the rate-type covariance constitutive structure with a finite set of the internal state variables.

The thermodynamic restrictions have been satisfied and the rate-type constitutive equations have been determined. Fracture criterion based on the evolution of the anisotropic intrinsic microdamage is formulated. The fundamental features of the proposed constitutive theory have been carefully discussed.

1. Prologue

Application of nanocrystalline metals, ceramics and composites in modern technology are recently multiplying rapidly. Nanocrystalline materials have been the subject of widespread investigations over the past couple of decades, with significant advancement in their processing as well as understanding of the mechanical properties and novel deformation mechanisms. Nanocrystalline materials are defined as those with their average and entire range of grain size, typically finer than 100 nm; ultrafine crystalline materials are defined as those with grain

sizes of the order of 100 nm – 1 μm; when one or more dimensions on average are smaller than 100 nm, the material is often termed "a nanostructured material". Comparison of the average grain size of crystalline materials with length of electromagnetic waves is shown in Fig. 1.

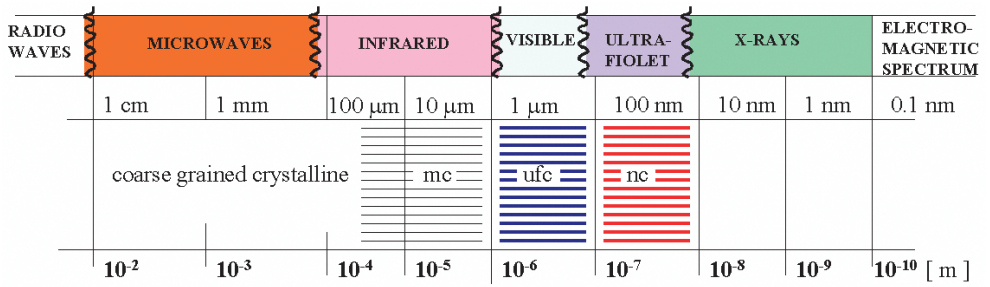

nc – nanocrystalline materials = with their average and entire range of grain size finer than 100 nm
ufc – ultrafine crystalline materials = with grain size on the order of 100 nm – 1 μm
mc – microcrystalline materials = with average grain sizes greater than 1 μm
ns – nanostructured materials = with one or more dimensions on average smaller than 100 nm

FIG. 1. Comparison of the average grain size of crystalline materials with length of electromagnetic waves.

The main objective of the present paper is the development of thermodynamical elasto-viscoplastic constitutive model describing the behaviour of nanocrystalline metals. Only *fcc*, *bcc* and *hcp* metals will be covered in this description, because they are the classes of metals for which systematic experimental observation data sets are available.

Experimental observations and physical foundations concerning the behaviour of nanocrystalline metals under quasistatic and dynamic loading are discussed. Analysis of strength, ductility, strain rate sensitivity, temperature dependence, strain-induced anisotropy, anisotropy of microdamage processes, microshear and macroshear banding, have been presented. Investigation of the deformation mechanisms is important for understanding, controlling and optimizing the mechanical properties of nanocrystalline metals.

Based on experimental observations we can suggest that intrinsic microdamage processes in nanocrystalline metals depend very much on the strain-rate effects. A microdamage process is treated as a sequence of nucleation, growth and coalescence of micro(nano)voids or micro(nano)cracks. The spacing of dimples, however for nanocrystalline metals, is considerably larger than the grain size in their specimen, cf. MEYERS *et al.* [24]. It is important to note that a microdamage process in nanocrystalline metals, is of a very anisotropic nature.

A set of internal state variables $\boldsymbol{\mu} = (\epsilon^p, \boldsymbol{\xi}, \boldsymbol{\alpha}, d)$ consists of two scalars and two tensors, namely the equivalent inelastic deformation ϵ^p, the second-order

microdamage tensor $\boldsymbol{\xi}$, with the physical interpretation that $(\boldsymbol{\xi} : \boldsymbol{\xi})^{1/2} = \xi$ defines the volume fraction porosity, the residual stress tensor (the back stress) $\boldsymbol{\alpha}$ and d – the mean grain diameter. The equivalent inelastic deformation ϵ^p describes the dissipation effects generated by viscoplastic flow phenomena, the microdamage tensor $\boldsymbol{\xi}$ takes into account the anisotropic intrinsic microdamage mechanisms on internal dissipation, the back stress tensor $\boldsymbol{\alpha}$ aims at the description of dissipation effects caused by the kinematic hardening, and d describes the dynamic grain growth during intensive deformation process.

2. Experimental observations

2.1. The behaviour of nanocrystalline metals under quasistatic loadings

Grain size is known to have a significant effect on the mechanical behaviour of materials. The yield stress for metals is increasing when the grain size is decreasing.

The compressive stress-strain curves for ultrafine-grained and nanocrystalline Cu, Fe, Ni and Ti are shown in Fig. 2, cf. Meyers *et al.* [25]. It is observed that work hardening saturates at a very low plastic strain. This is a strong predictor for shear instability, since there are three key elements dictating shear localization: thermal softening, which favors shear localization, and strain-rate sensitivity and work hardening, which oppose shear localization. For nanocrystalline *bcc* metals, the three effects drive shear band formation, and it is indeed prevalent.

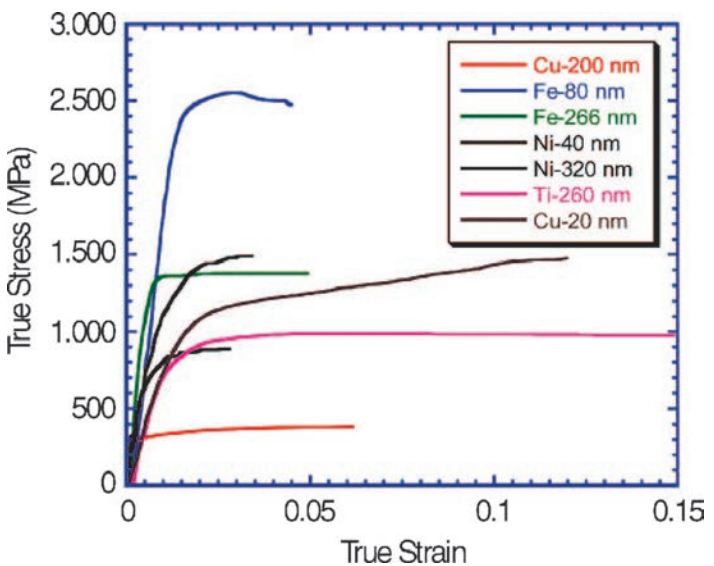

Fig. 2. The compressive stress-strain curves for ultrafine-grained and nanocrystalline Cu, Fe, Ni and Ti (data from several sources), cf. Meyers *et al.* [25].

Figure 3a shows an engineering stress-strain curve of nanocrystalline Cu (the average d is 54 nm) after RT milling for 5 h following the LN_2T milling, cf. Cheng *et al.* [4]. The material exhibits a 0.2% offset yield strength of ∼688 MPa. Since the cross-sectional area remained approximately uniform along the gage length during straining, the engineering stress-strain curve was converted into a true stress-strain curve using a standard formula, Fig. 3b, which illustrates an elastic-nearly perfectly plastic behaviour with a total strain of 0.06. The stress-strain curve may be divided into three regions. Region I corresponds to elastic deformation. In Region II, some strain hardening is present and the deformation is uniform across the gage length. The subsequent strain-hardening rate is low because the grains are so small, or already saturated with defects, such that dislocation pile-ups and cell structures cannot develop the same way as that known for coarse-grained Cu. This is followed by Region III, where the stress levels off to a nearly perfectly plastic behaviour that can lead to shear instabilities.

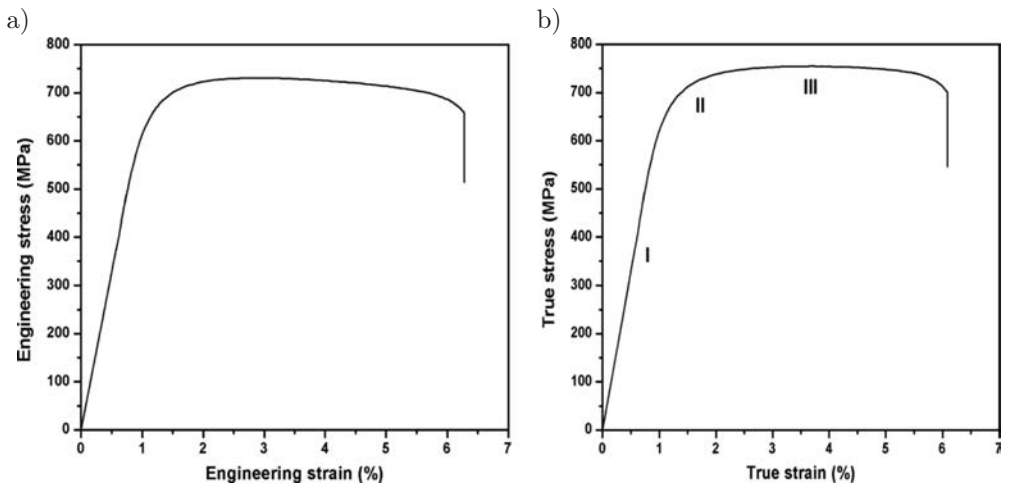

Fig. 3. Tensile engineering (a) and true (b) stress-strain curves of nc-Cu at RT. The strain rate is 10^{-4} s^{-1}. The samples were ball-milled at LN_2T for 3 h and RT for 5 h, cf. Cheng *et al.* [4].

Wang and Ma [52] investigated experimentally cryo-rolled UFG Cu (with sizes of grains in the 200–300 nm range). The tensile engineering stress-strain curve of this Cu is unstable, cf. Fig. 4, and peaks quickly at low strains and then plunges, in sharp contrast to that for coarse-grained Cu presented in the same figure that goes through stages of work hardening.

Youssef *et al.* [60] made experimental observations of artifact-free bulk nanocrystalline Cu with a narrow grain size distribution (mean grain size of 23 nm). From Fig. 5 we can see that this Cu exhibits tensile yielded strength,

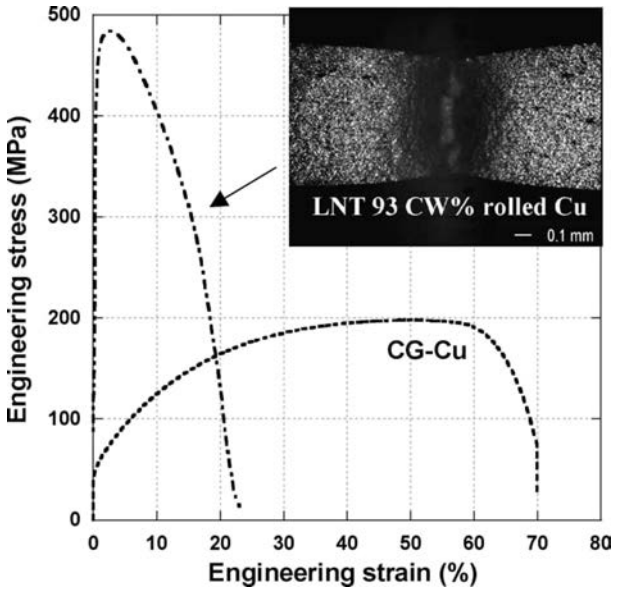

FIG. 4. Tensile engineering stress-strain curve of cryo-rolled Cu compared with that of coarse-grained Cu. The neck developed in the former sample is shown in the inset, cf. WANG and MA [52].

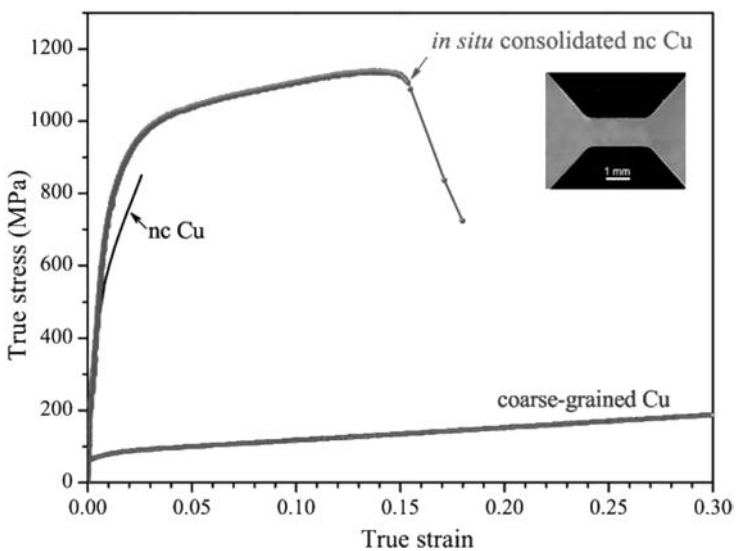

FIG. 5. A typical tensile true stress-strain curve for a bulk *in situ* consolidated nanocrystalline Cu sample (with an average grain size of 23 nm) with high purity and high density in comparison with that of coarse-grained polycrystalline Cu sample (with an average grain size larger than 80 μm) and a nanocrystalline Cu sample (with a mean grain size of 26 nm), prepared by an inert-gas consolidation and compaction techniques, cf. YOUSSEF *et al.* [60].

about 11 times higher than that of conventional coarse-grained copper, while retaining a 14% uniform tensile elongation.

Jia, Ramesh and Ma [16] studied the mechanical behaviour of consolidated iron with average grain sizes from tens of nanometers to tens of microns, under uniaxial compression over a wide range of strain rates. The solid lines in Fig. 6

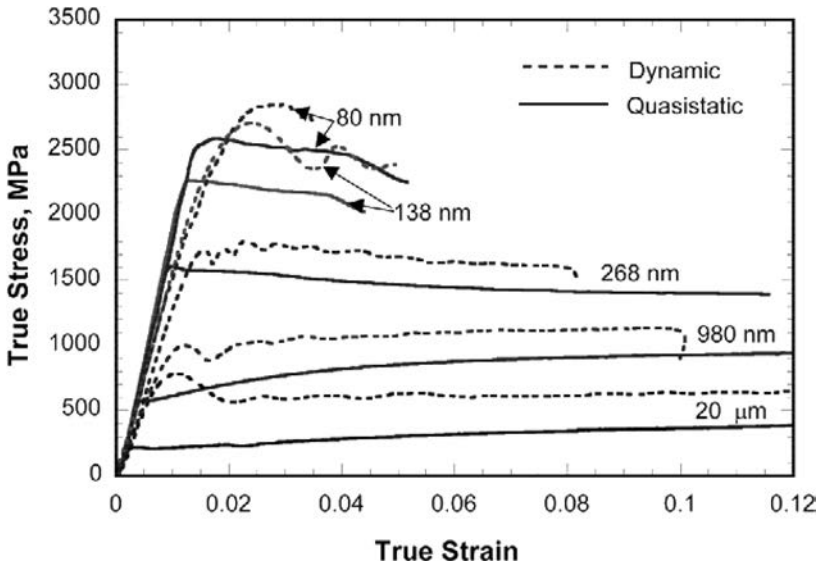

Fig. 6. Typical stress-strain obtained for the consolidated iron under quasistatic $(1 - 4 \times 10^{-4}\ \mathrm{s}^{-1})$ and high-strain-rate $(3 - 6 \times 10^{3}\ \mathrm{s}^{-1})$ uniaxial compression for all of the grain sizes, cf. Jia, Ramesh and Ma [16].

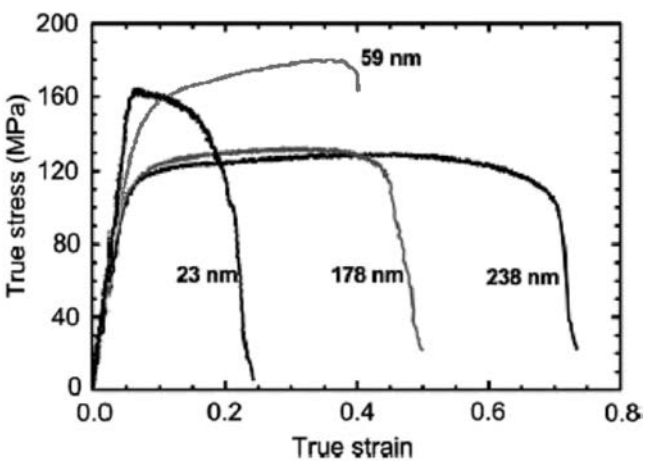

Fig. 7. Reduction of ductility as grain size is reduced for ball milled Zn tested at a constant strain rate of $10^{-4} - 10^{-3}\ \mathrm{s}^{-1}$ at room temperature, cf. Zhang *et al.* [61].

shows the true stress-strain curves of the consolidated iron with various average grain sizes obtained from the quasi-static compression tests. It is apparent that the yield strength (or flow stress) increases with decreasing grain size. Compared with the 20 μm Fe, the strength of the nano-Fe (80 nm) is increased by one order of magnitude. The strain hardening rate (the slope of the stress-strain curve) changes with the grain size. Ductile behaviour is observed at relatively large grain sizes, the samples with grain sizes smaller than 200 nm fail relatively early (the stress-strain curves presented end because of specimen failure).

Figure 7 shows the mechanical response of nanocrystalline zinc samples with different grain sizes. There is a significant drop in ductility as the grain size goes down from 238 nm to 23 nm.

2.2. Yield strength

Strengthening with grain size refinement in metals and alloys, with an average grain size of 100 nm or larger, has been characterized by the Hall-Petch (H-P) relationship, where dislocation pile-up against grain boundaries along with other transgranular dislocations mechanisms, are the dominant strength-controlling processes. When the average and entire range of grain sizes is reduced to less than 100 nm, the dislocation operation becomes increasingly more difficult and grain boundary-mediated processes become increasingly more important.

The dependence of yield stress on grain size in metals is well established in the conventional polycrystalline range (micrometer and larger sized grains). Yield stress, σ_y, for materials with grain size d, is found to follow the Hall-Petch relation

$$\sigma_y = \sigma_o + kd^{-1/2}, \tag{2.1}$$

where σ_0 is the friction stress and k is a constant. This is an approximation, and a more general formulation is to use a power expression with exponent $-n$, i.e.

$$\sigma_y = \sigma_o + kd^{-n}, \tag{2.2}$$

where $0.3 \leq n \leq 0.7$.

The Hall-Petch trends for a range of grain sizes from the micro to the nanocrystalline, are plotted in Fig. 8 for four different metals: Cu, Fe, Ni and Ti, cf. MEYERS *et al.* [24]. Data points have been collected from different sources for grain sizes ranging from a micrometer to the nanometer range. The authors pointed out that the data points in the conventional polycrystalline range for most of these plots overlap while they are more spread out in the nanocrystalline

range. The Hall-Petch curve for the nanocrystalline range clearly shows a deviation from the regular trend in the microcrystalline range. However, there is no clear evidence on the nature of the curves at grain sizes below 15 nm.

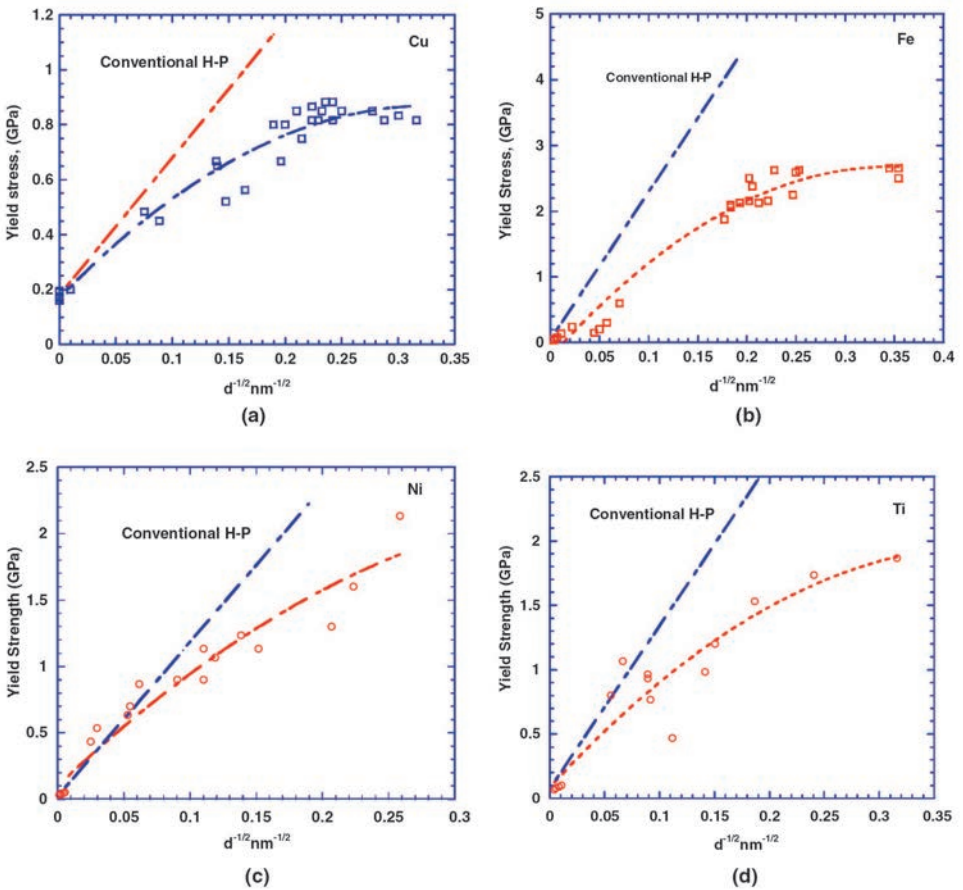

FIG. 8. Plots showing the trend of yield stress with grain size for different metals as compared to the conventional Hall-Petch response: (a) copper, (b) iron, (c) nickel and (d) titanium, cf. MEYERS *et al.* [24].

The difficulty in making realistic predictions of the strength of nanocrystalline metals based on experiments is illustrated by the results presented by MEYERS *et al.* [25] in Fig. 9. This figure represents a compilation of data from several sources for copper. This plot is of the Hall-Petch type, albeit with the abscissa in nanometer units. Although for larger grain sizes the linearity is clear, for grain sizes of 100 nm or larger ($d^{-1/2} > 0.1$ nm$^{-1/2}$) there is no clear trend. While some results show a decrease in the yield stress (negative Hall-Petch slope), some

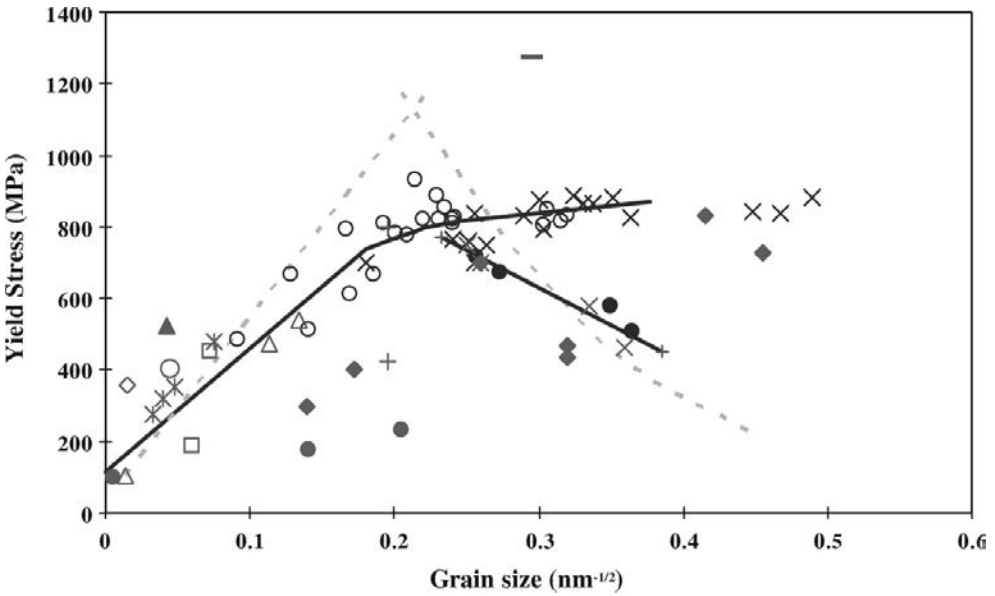

FIG. 9. The compiled yield stress versus grain size plot for copper from various sources ranging from coarse to nanograin size. The plots show different trend as the grain size falls below a critical size, cf. MEYERS *et al.* [25].

show an increase (positive Hall-Petch slope, albeit of a lower magnitude), and others still a plateau.

2.3. The behaviour of nanocrystalline metals under dynamic loadings

SCHWAIGER *et al.* [47] systematically changed the loading rate and strain rate during controlled identification of electrodeposited nc Ni (average grain size ∼40 nm) and showed that the flow stress of samples was highly sensitive to the rate of deformation. Their results are reproduced in Fig. 10.

WANG and MA [52] for the Cu discussed in Subsec. 2.1 determined (in compression tests) the strain rate sensitivity. Figure 11a shows results of the tests at various fixed strain rates, using several different samples. Figure 11b, instead, uses repeated loading, unloading and reloading to observe effects of strain rate jumps on the flow stress for a given microstructure, so that the deformation process can be separated from the kinetics of microstructure evolution.

Figure 12 displays the engineering stress-strain curves of the 6 h RT-milled nc-Cu tested at different strain rates, ranging from 10^{-4} to 10^{-2} s^{-1}, cf. CHENG *et al.* [4]. Compared to Fig. 3, the curve with a rate of 10^{-4} s exhibits a larger elongation (∼12%), but at the expense of some strength. This decreased strength can be attributed to a coarsened average grain size (average $d = 62$ nm) as

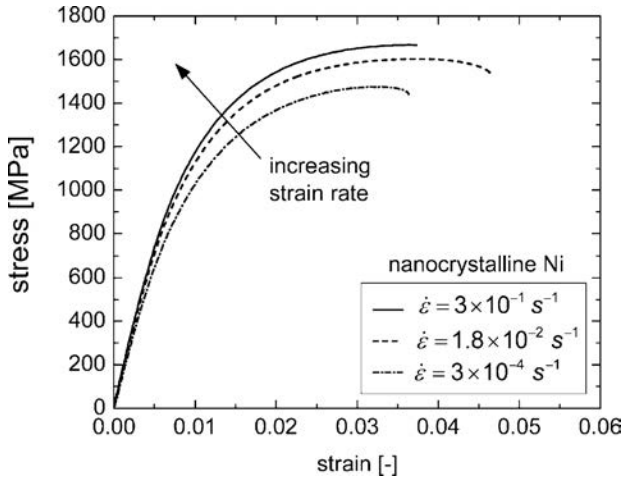

FIG. 10. Engineering stress-strain curves of an electrodeposited nanocrystalline Ni with an average grain size of 40 nm, obtained from tensile tests at different strain rates, cf. SCHWAIGER *et al.* [47].

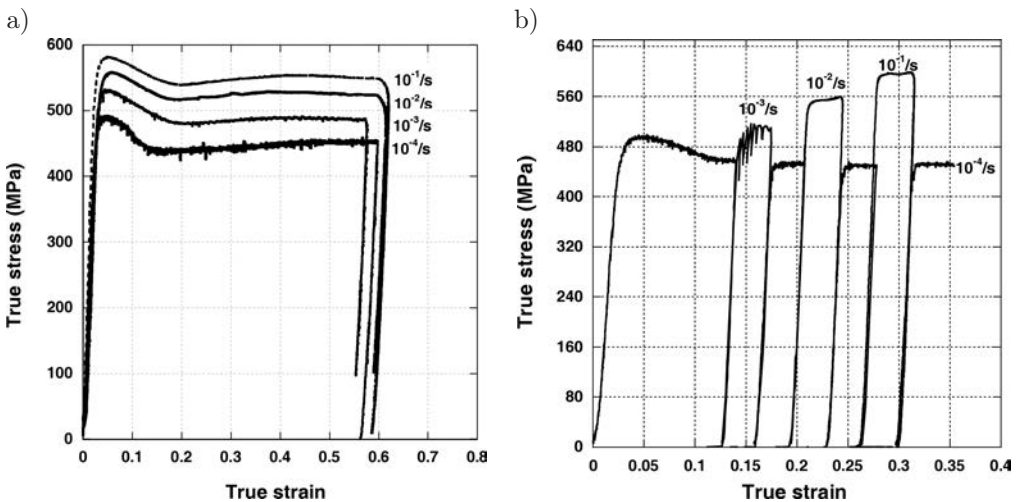

FIG. 11. (a) Compressive true stress-true strain curves of cryo-rolled Cu at several different strain rates and (b) a repeated loading-unloading-reloading compressive test curve for the cryo-rolled Cu to determine the strain rate sensitivity through rate jumps, cf. WANG and MA [52].

a result of the longer RT ball milling. One salient feature in Fig. 12 is the increased strength at higher strain rates. The elongation, however, decreases with the strain rate. The strain rate sensitivity of the flow stress, defined as

$$m = \left.\frac{\partial \log \sigma}{\partial \log \dot{\epsilon}}\right|_{\epsilon,\vartheta}, \tag{2.3}$$

where σ is the flow stress and $\dot{\epsilon}$ the corresponding strain rate, was estimated to be ∼0.027 from the flow stress data at a fixed strain of 2.5%, as shown in the inset of Fig. 12. The magnitude of m seen here represents a fourfold increase over that of conventional coarse-grained Cu ($m = 0.006$), cf. Wang and Ma [52].

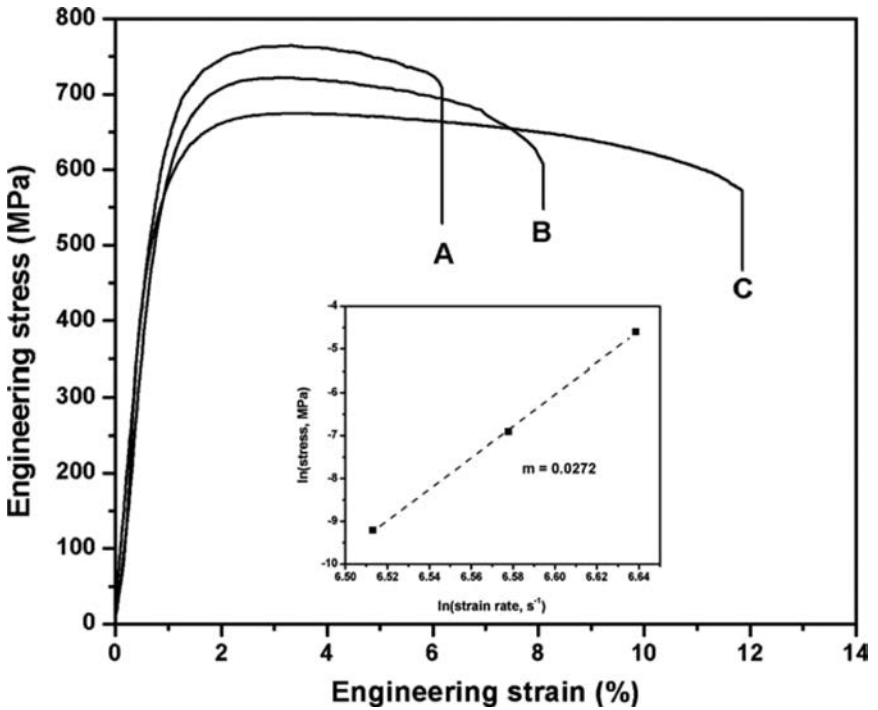

Fig. 12. Tensile test of nc-Cu at RT with different strain rates: A – $\dot{\epsilon} = 10^{-2}$ s^{-1}; B – $\dot{\epsilon} = 10^{-3}$ s^{-1}; C – $\dot{\epsilon} = 10^{-4}$ s^{-1}. The inset is used to estimate the strain rate sensitivity, m. The samples were ball milled at LN_2T for 3 h and RT for 6 h, cf. Cheng *et al.* [4].

Figure 6 (cf. Jia, Ramesh and Ma [16]) also shows a set of stress-strain responses at high strain rates of $3 \times 10^3 - 6 \times 10^3$ s^{-1} (the dashed lines), for the consolidated iron for several grain sizes. Strain-rate hardening is evident for all the grain sizes considered. Small influence of the strain rate on the strain hardening (the slope of the curves) is observed, which is typical for *bcc* metals. The ends of the high-rate stress-strain curves for the smallest two grain sizes represent specimen failures. The influence of the rate of deformation on the flow stress is plotted in Fig. 13 for the entire range of grain sizes and strain rates, using a conventional semi-log format, with the flow stresses, corresponding to a fixed strain of 4%.

Wei *et al.* [56] investigated the plastic deformation behaviour of ultrafine-grained (UFG) bulk Fe. The UFG microstructure (grain size) ∼300 and ∼150 nm,

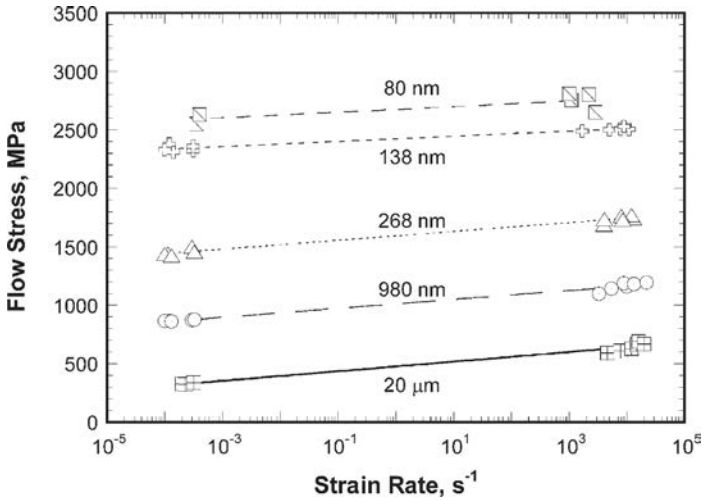

FIG. 13. Rate dependence of the flow stress of the consolidated iron for each grain size, with the flow stresses plotted at a fixed strain of 4%, cf. JIA, RAMESH and MA [16].

was obtained through combined equal channel angular extrusion (ECAE) and low-temperature rolling (ECAE+R), and confirmed using the transmission electron microscopy.

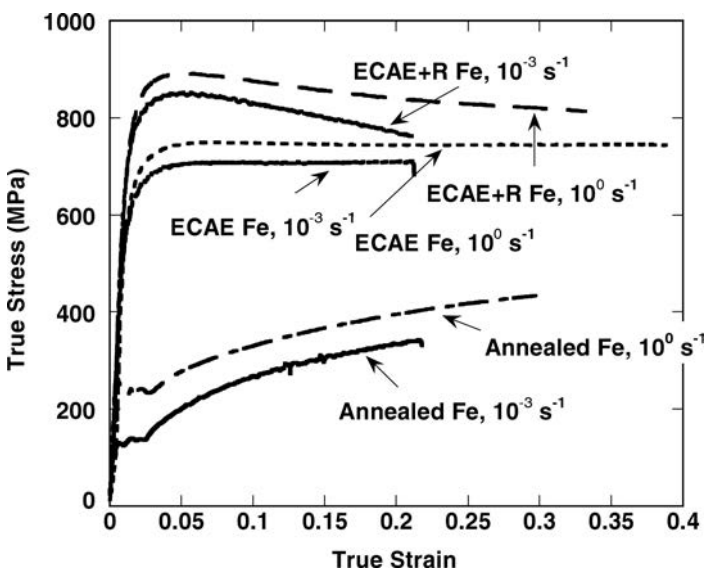

FIG. 14. Quasi-static stress-strain curves under compressive loading for Fe in annealed, ECAE processed, and ECAE+R conditions. Note the significant strain hardening in the annealed Fe which is absent in the SPD processed Fe. Also note the apparently reduced rate dependence in the SPD Fe. The strain rates are given in the figure, cf. WEI *et al.* [56].

Figure 14 presents the true stress-strain curves obtained during quasi-static compressive loading of the annealed Fe as well as the ECAE Fe and the ECAE+R Fe. The annealed material exhibits strain hardening typical for the *bcc* Fe, but the yield strength is higher than the ∼50 MPa known for high-purity Fe. The ECAE Fe behaves in a nearly elastic-perfectly plastic manner at these strain rates (i.e., little strain hardening is observed). Yield strengths above 600 MPa are observed, with the strength increasing slightly with the strain rate. It is seen that the yield strength of the ECAE Fe is further increased by about 200 MPa after low-temperature rolling (see curves for ECAE+R Fe). Apart from the absence of strain hardening, in this case, some slight flow softening is in fact present.

Figure 15 displays the stress-strain curves obtained under dynamic loadings. The annealed Fe exhibits significant strain hardening to a strain level of 0.2, and after that, the stress-strain curve levels off because of adiabatic heating and subsequent dynamic recovery and recrystallization. After ECAE processing the strength is increased by a factor of approximately 2, accompanied by slight flow softening. In the case of ECAE+R Fe, the yield strength is further enhanced by

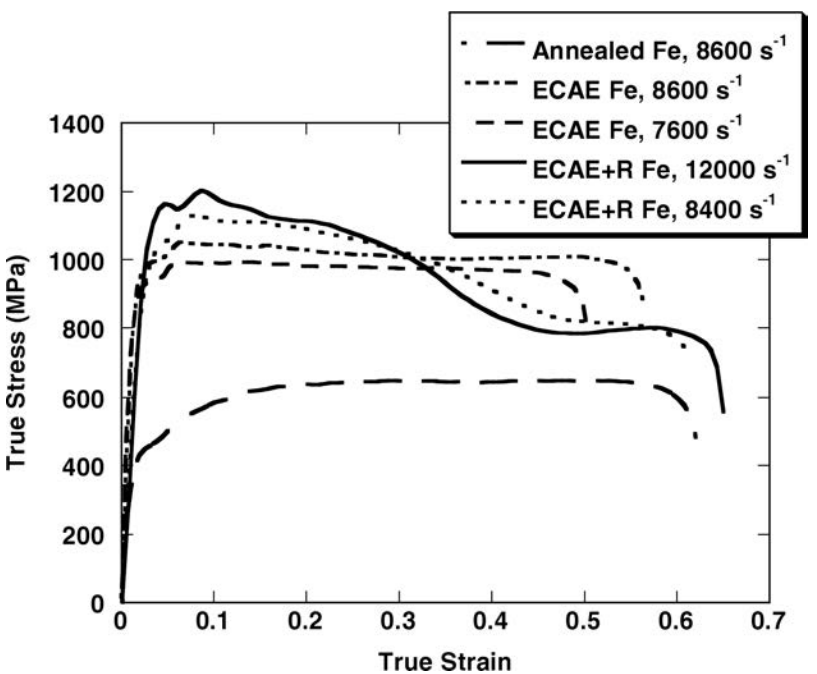

Fig. 15. Dynamic stress-strain curves from Kolsky bar compression tests for Fe in the annealed, ECAE, and ECAE+R conditions. Note the strain hardening in the annealed Fe to a strain of 0.2. The strain hardening is absent in the SPD processed samples. On the contrary, flow softening is observed in these samples, in particular in the ECAE+R state. The strain rates are given in the figure, cf. Wei *et al.* [56].

$\sim$150 MPa compared to the ECAE Fe. What is striking is that the ECAE+R Fe exhibits much more pronounced flow softening in comparison with the ECAE Fe. Similarly to the ECAE Fe, the rate dependence of the flow stress is reduced compared to the annealed state.

2.4. Strain rate sensitivity and temperature dependence of yield strength

The strain rate and temperature dependence of strength have been found to be rather in nc or ns metals, more so than it had been realized previously.

The engineering parameter measuring strain-rate sensitivity m is one of the key engineering parameters for controlling and understanding of the deformation in nanocrystalline metals. For example, a highly strain rate sensitive material is expected to resists localized deformation and hence be ductile.

With decreasing grain size, an increase in the strain rate sensitivity has been found to be common for nanocrystalline *fcc* metals, cf. Dao *et al.* [7]. For the behaviour of nanocrystalline *bcc* metals the situation is different, and more complex, cf. Jia *et al.* [16].

Dao *et al.* [7] summarized the variation of m as a function of grain size, d, for Cu samples, based on literature data. The m value increases with a decrease of grain size from the micron to the submicrometer scale (m from 0.06 to about 0.02), followed by an obvious rise when the grain sizes are reduced to below a couple of hundred nanometers.

In the nanoscale regime, m is much larger than that reported for conventional Cu. The current suggestion is that the highly localized dislocation activity (e.g. dislocation nucleation and/or dislocation de-pinning) at the grain boundaries, leads to an enhanced strain-rate sensitivity for nanocrystalline metals.

The overall strain-rate dependence of a material is influenced by dislocation activity, grain boundary diffusion and lattice diffusion. For microcrystalline *fcc* metals, the rate-controlling process is the cutting of forest dislocations resulting in a low strain-rate sensitivity. With d decreasing into submicrometer and nanocrystalline regime, forest cutting mechanisms subside since now it is the large number of grain boundaries and/or subgrain boundaries that serve as obstacles to the dislocation motion. The rate-limiting process is increasingly influenced by dislocation-grain boundary interactions.

There have been indications that the elevated strain rate sensitivity m in nc/ns metals plays a role in improving the strength/ductility properties. The strength increase due to the rate sensitivity is seen in Fig. 10.

The general trend of increasing of the strain-rate sensitivity m occurs with decreasing d for *fcc* nanocrystalline metals from the known data for Cu in Fig. 16a and Ni in Fig. 16b, as well as in Fig. 17a for Cu and Ni. For *bcc* nanocrystalline metals, the strain-rate sensitivity m shows an opposite dependence on grain size.

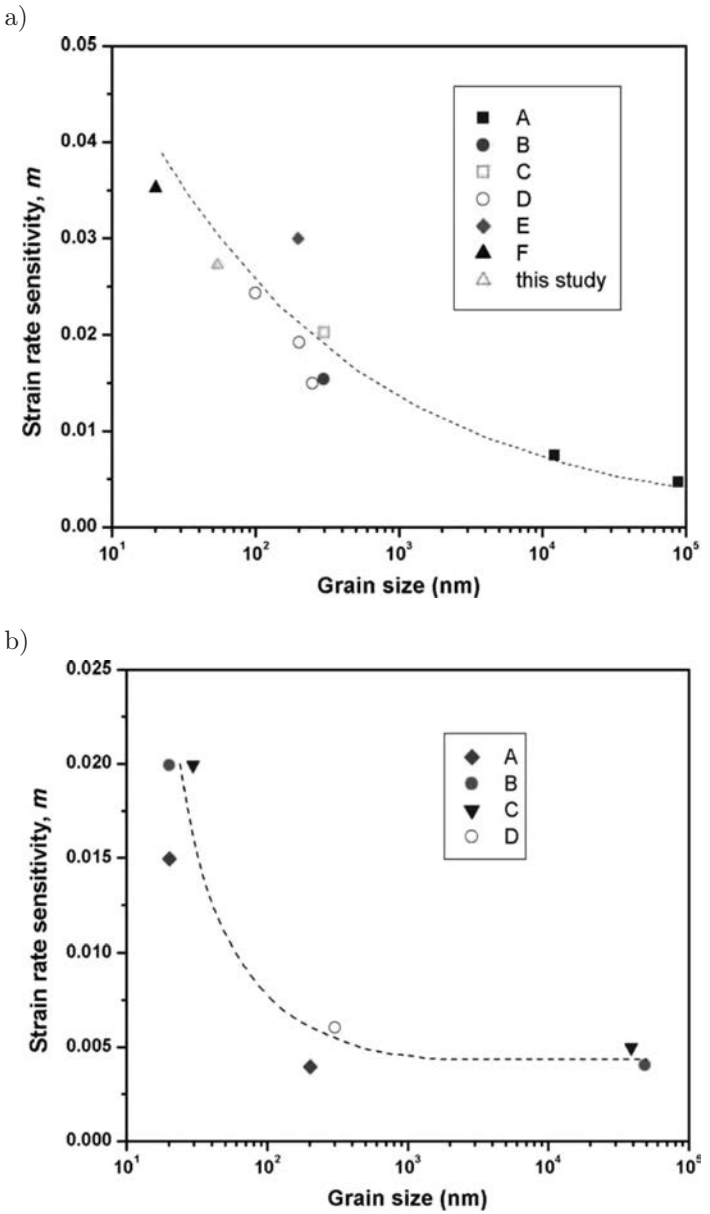

FIG. 16. Summary of strain rate sensitivity m vs. grain size d for Cu (a) and Ni (b) from literature. In both cases, m shows an increasing trend as d decreases. The dashed curves serve as guide to the eye, cf. CHENG *et al.* [4].

The result for Fe, Ta, V and W are shown in Fig. 17b. Similar results have been obtained in experimental observations of UFG/nc-Fe by JIA *et al.* [16] these data are illustrated in Fig. 18, and by WEI *et al.* [56], see Fig. 19.

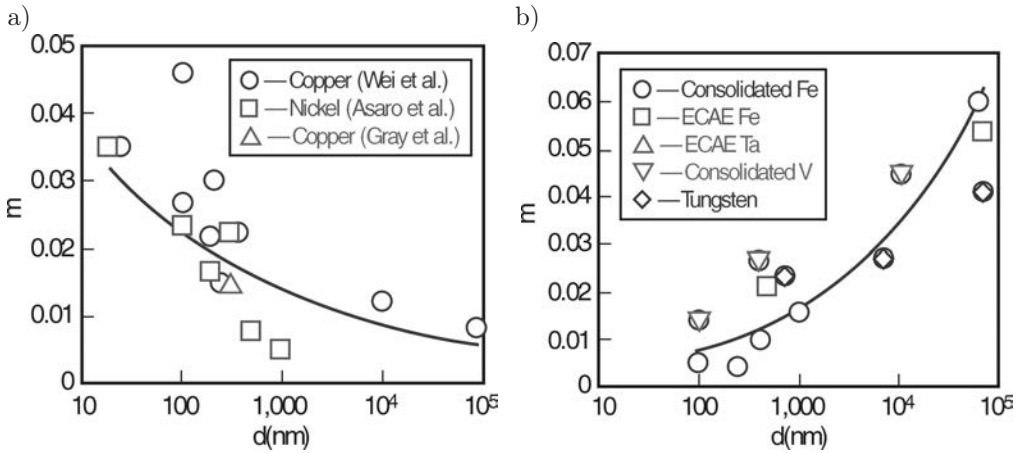

FIG. 17. The strain-rate sensitivity as a function of grain size for: a) *fcc* metals: Cu and Ni; b) *bcc* metals: Fe, Ta and W, cf. MEYERS *et al.* [25].

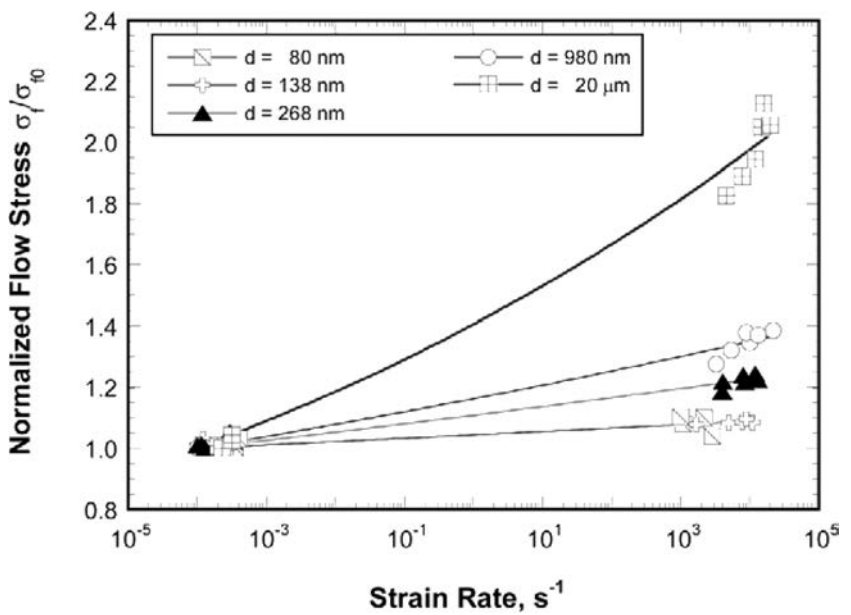

FIG. 18. The variation of the normalized flow stress σ_f/σ_{f_0} with strain rate for various grain sizes. Note the reduction in the effective rate sensitivity at the smaller grain sizes, cf. JIA, RAMESH and MA [16].

These important differences for the dependence of the strain-rate sensitivity parameter m on grain size for *fcc* and *bcc* ns-metals are caused by various rate-controlling mechanisms. The rate-controlling mechanism for *fcc* ns-metals is cutting of dislocation forests by a moving dislocation, while for *bcc* nc-metals it

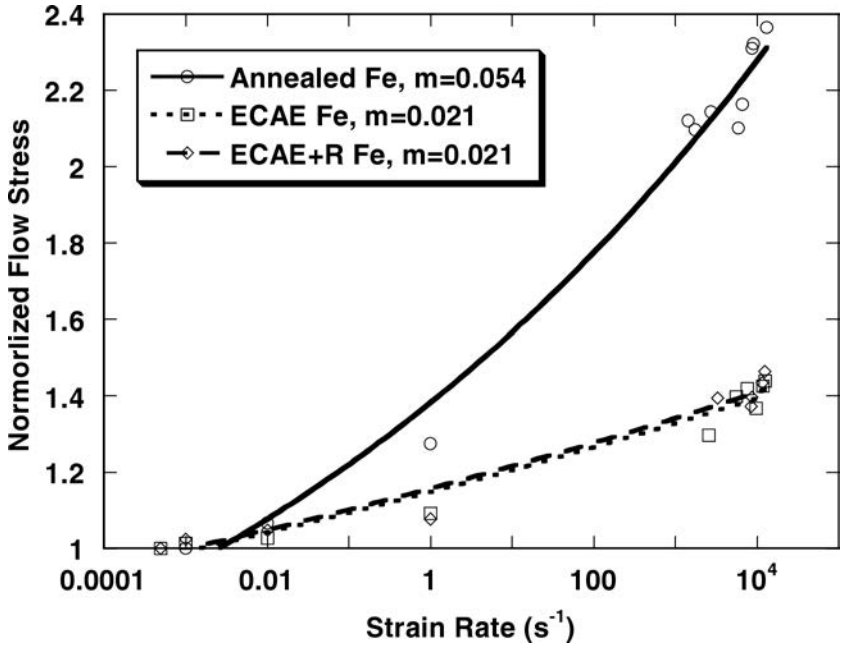

FIG. 19. Rate dependence of different states of Fe. The values of the strain rate sensitivity, m, are given in the figure. Note the substantial reduction in m in the SPD processed Fe in comparison to the annealed state, cf. WEI *et al.* [56].

is the thermally activated motion of screw dislocations by the Seeger kink-pair lateral movement and this is controlled by Peierls-Nabarro stresses.

Very interesting results were presented by WANG and MA [52] for cryo-rolled UFG Cu (with sizes of grains in the 200–300 nm range), cf. Fig. 20. They showed that for the strain-rate range used, the m is 0.03–0.04 which is higher than that for conventional Cu (0.01). We can also observe the important difference of the strain-rate sensitivity parameter m for the load-unload test, in comparison to the simple loading test.

Corresponding to the enhanced strain-rate dependence, there is also a more pronounced temperature dependence, arising from the thermally activated deformation mechanisms controlling the plastic flow. A rapid increase in yield strength has been documented for nc Ni and nc Cu, when the deformation temperature is lowered to below the room temperature. This feature could be useful for cryogenic applications.

CHENG *et al.* [4] reported strong temperature dependence of the flow stress *in situ* consolidated nanocrystalline Cu and explained the results in terms of the thermally activated deformation mechanism operative in the nanocrystalline grains. In Fig. 21 we observe the large jump in the yield strength from RT to 77 K.

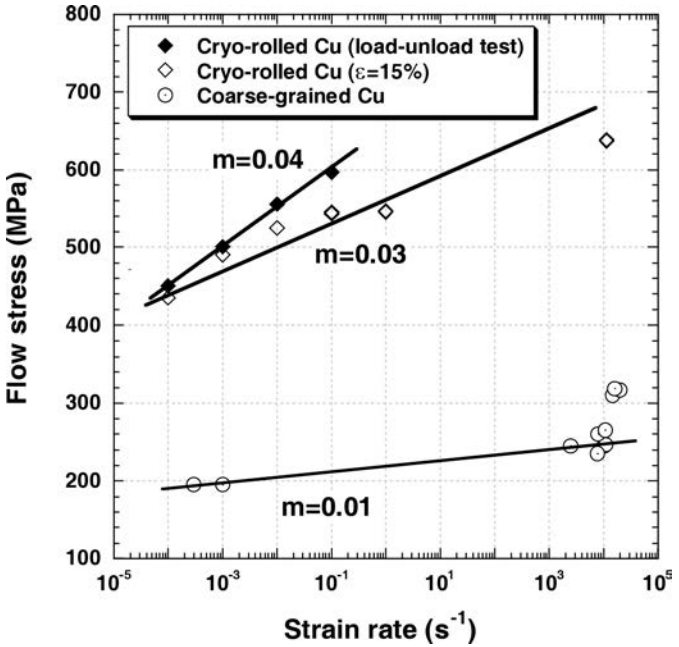

FIG. 20. Flow stress vs. strain rate plot for the cryo-rolled Cu compared with that for conventional Cu. The strain rate sensitivity m has been determined from double-log plots (not shown), cf. WANG and MA [52].

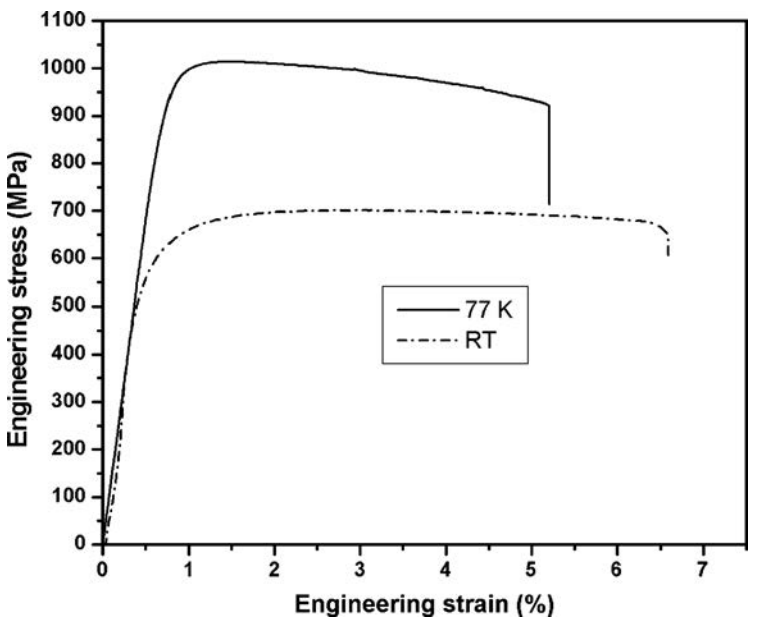

FIG. 21. Tensile test of nc-Cu at RT and 77 K, with a strain rate $\dot{\epsilon} = 10^{-4}$ s^{-1}; the samples were ball-milled at LN_2T for 3 h and RT for 6 h, cf. CHENG *et al.* [4].

EBRAHIMI *et al.* [11] investigated nickel foils with nano-size grains in tensile tests at room temperature and −196°C. Figure 22 presents the stress-strain curves for two different grain sizes tested at room and liquid nitrogen temperature. Decreasing of test temperature increased the strength significantly. Nickel has a high stacking fault energy and therefore, its strain hardening rate is expected to be relatively temperature insensitive. However, the smaller grain size specimen showed a noticeable increase in the strain hardening rate with reducing the test temperature. The increase in strength was also more significant for the smaller grain size specimen.

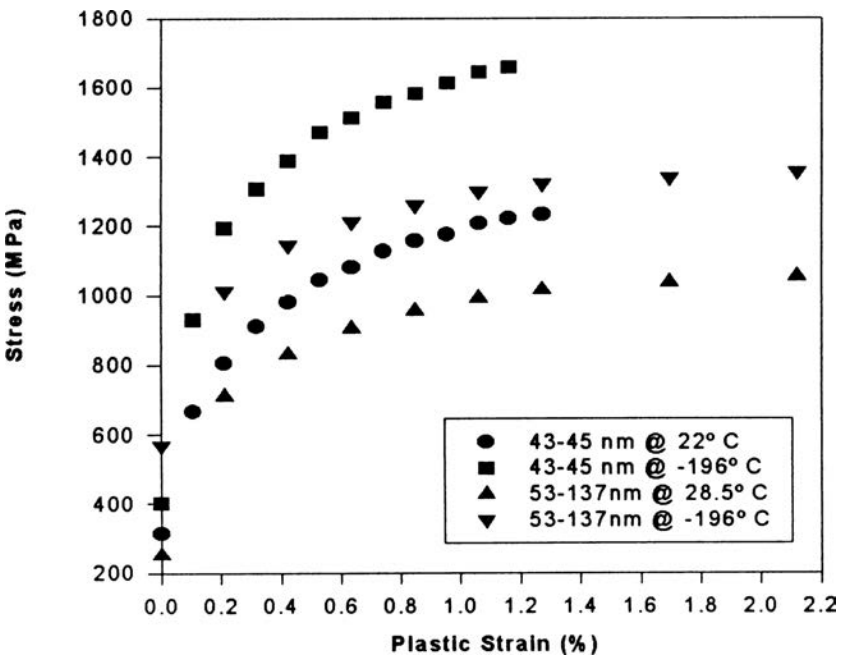

FIG. 22. Effect of grain size on tensile stress-strain curves of nickel at RT and liquid nitrogen temperature, cf. EBRAHIMI *et al.* [11].

2.5. Analysis of microshear and macroshear banding

JIA, RAMESH and MA [16] presented analysis of phenomenology of shear bands in UFG and nc Fe. They observed that the deformation mode of these materials changed dramatically as the grain size was decreased into the ultrafine-grain range. In the 20 μm-Fe and 980 nm-Fe, the compressive deformations were uniform at all strain rates, and no shear bands were evident under either the optical microscope or SEM. However, for all smaller grain sizes ($d < 300$ nm) the shear band localization development is often observed to occur immediately after the onset of plastic deformation. This has been correlated to changes in strain

hardening behaviour at those grain sizes, since the ability to work hardened by the increase in dislocations density is lost.

Shear bands were observed during both the quasistatic and high-rate deformations for these grain sizes. Comparative optical micrographs are presented in Fig. 23 after low-rate compressive deformations to similar plastic strains, showing (a) the uniform deformations in the 980 nm-Fe and (b) the strongly non-uniform deformations in the 268 nm-Fe. In both cases, the microshear is visible. Figure 23c shows the strongly non-uniform deformations observed in the 268 nm-Fe after high-rate loading to a similar strain as those shown in Figs. 23a and 23b.

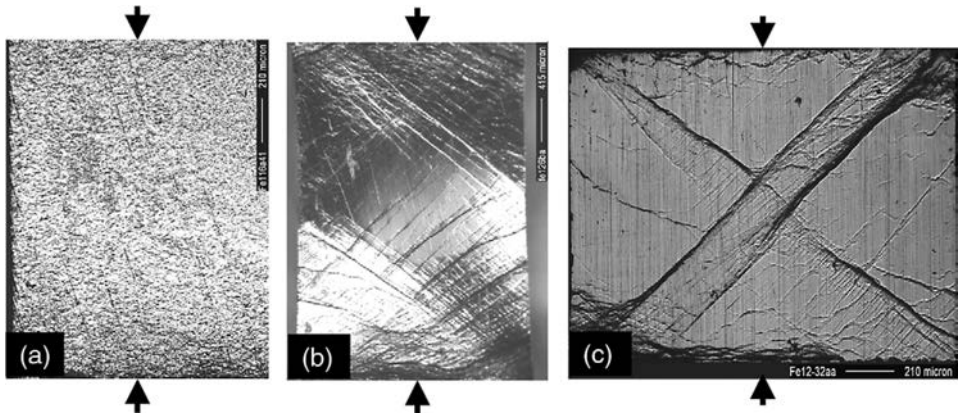

FIG. 23. Change in deformation mode of consolidated iron with grain size for uniaxial compression: a) uniform low-rate deformations with $d = 980$ nm, $\epsilon = 13.7\%$; b) non-uniform low-rate deformations with $d = 268$ nm, $\epsilon = 11.6\%$ and c) non-uniform high-rate deformations with $d = 268$ nm, cf. JIA, RAMESH and MA [16].

The process of macroshear banding that develops during a quasistatic experiment can be observed in Fig. 24, which shows a single area (far away from the edges) of a 268 nm-Fe specimen at nominal plastic strains of (a) 3.7% and (b) 7.8%. The loading axis is vertical in these figures. Authors suggested, basing on observations with optical microscopy and TEM for the deformed UFG and nc-Fe specimens, that large plastic deformations are developed within the bands. Thus, it appears that the process of macroshear banding in this material involves the nucleation of new bands, propagation along the shear plane, increase in width (broadening) and increase in strain (flow) within the band.

Figure 25a shows a high magnification view of a simple band with well-defined boundaries (this band was observed at a nominal plastic strain of 0.3%, just after yield in the 268 nm-Fe). The measured width of the macroshear band is $\sim$16 μm and the shear strain in the band is $\sim$25% (nearly two orders of magnitudes higher than the nominal specimen strain).

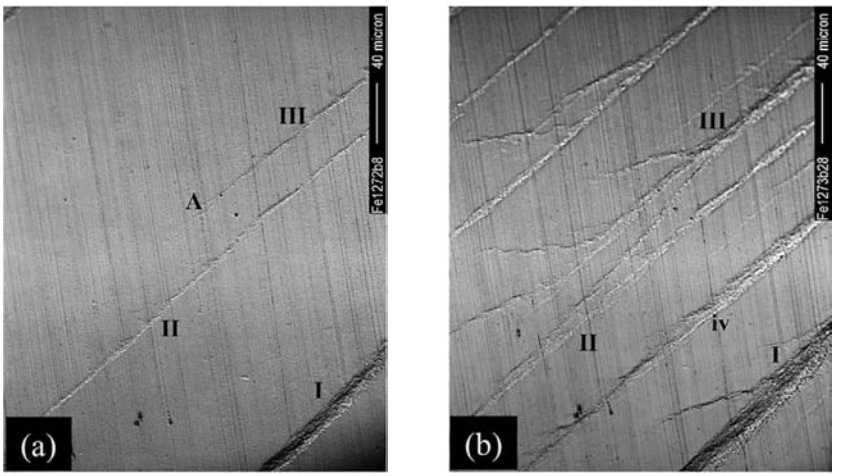

FIG. 24. Evolution and development of shear bands in 268 nm-Fe. Observations of shear bands at the same location at different nominal strain levels: a) 3.7%; b) 7.8%. Loading axis is vertical. Note the development of new shear bands, the broadening of existing shear bands, and the propagation of a shear band tip, cf. JIA, RAMESH and MA [16].

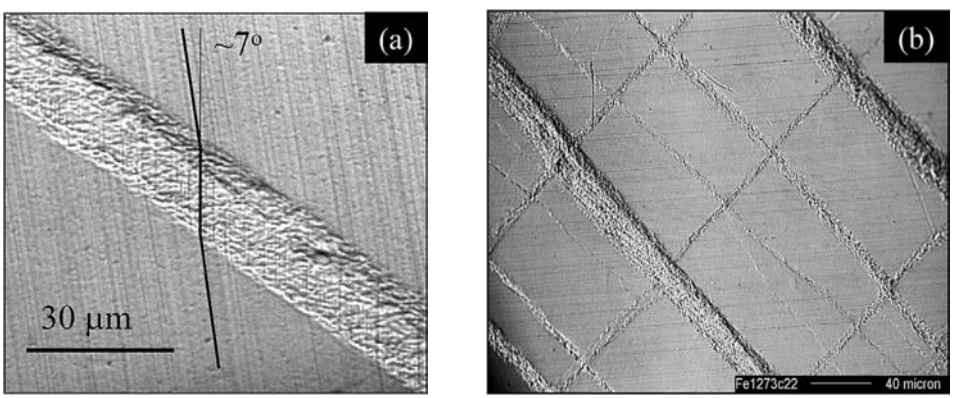

FIG. 25. a) Shear strain developed in shear band immediately after onset of plastic deformation (0.3% plastic strain) in 268 nm-Fe under uniaxial compression, b) Shear band network formed in 268 nm-Fe after uniaxial compression at low rates to 7.8%. Note the compatible deformations at the intersections of the shear bands, cf. JIA, RAMESH and MA [16].

Figure 25b shows a network of macroshear bands at about $\pm 45°$ to the loading axis in a 268 nm-Fe specimen after low-rate loading to 7.8% of the nominal plastic strain. For most of the bands, the two boundaries can be clearly identified, so that the width can be accurately measured. Wider bands were observed in the 268 nm-Fe than in 138 or 80 nm-Fe. An example of the TEM results is presented in Fig. 26, which shows TEM micrographs obtained from within and

outside the macroshear bands in the 110 nm-Fe, deformed in compression at low rates. Figure 26a is a typical picture obtained from within the macroshear band, and shows elongated grains (elongated along the shearing direction) containing high dislocation densities. Figure 26b was obtained from a region outside the macroshear bands.

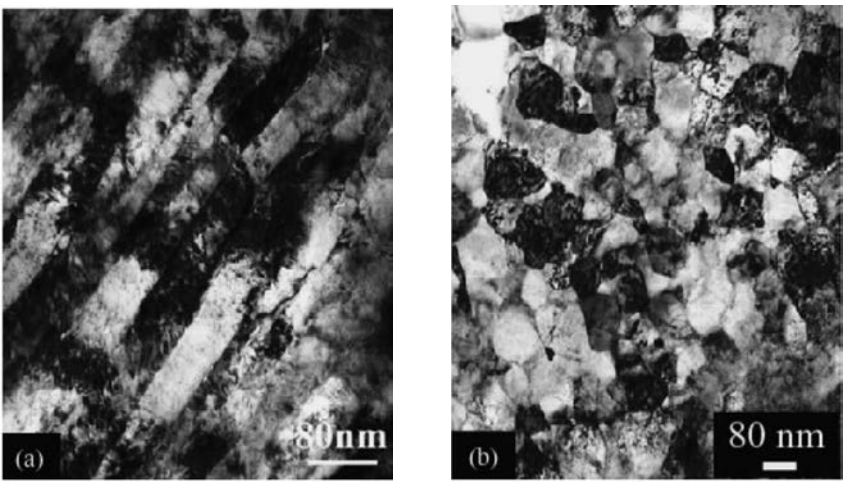

FIG. 26. TEM micrographs taken within (a) and outside (b) a shear band in 138 nm-Fe. Note the equiaxed grains outside the band, and the elongated grains in the band oriented along the shear direction, cf. JIA, RAMESH and MA [16].

WEI *et al.* [56] have been shown that under dynamic loading, the plastic flow mode changes from the uniform deformation of conventional coarse-grained Fe to substantial, localized deformation in UFG Fe. They observed that ECAE processed Fe did exhibit signs of localized deformation under dynamic compressive loading. Figure 27 depicts the concentrated shear in local regions of one of the samples (loading is along the vertical direction). The specimen was loaded to a true strain level of $\sim$0.55 at a strain rate of $\sim$7000 s^{-1}. Figure 27a shows the low magnification SEM image of the shear marks on the surface of the sample. Figure 27b shows an overall view of some of the shear lines. More detailed structure of the shear lines is revealed in Fig. 27c.

Figure 28 shows the post-dynamic loading SEM images of the ECAE+R Fe. The specimen was loaded to a true strain level of $\sim$0.6 at a strain rate of around 8000 s^{-1}. In this case, macroshear banding is ostensive. The low magnification SEM micrograph in Fig. 28a shows two major macroshear bands. Figure 28b is an enlarged image of the left band in Fig. 28a, with details of the areas indicated by arrows given in Fig. 28c–f. These images demonstrate that the macroshear bands have accommodated highly concentrated strain and local adiabatic temperature

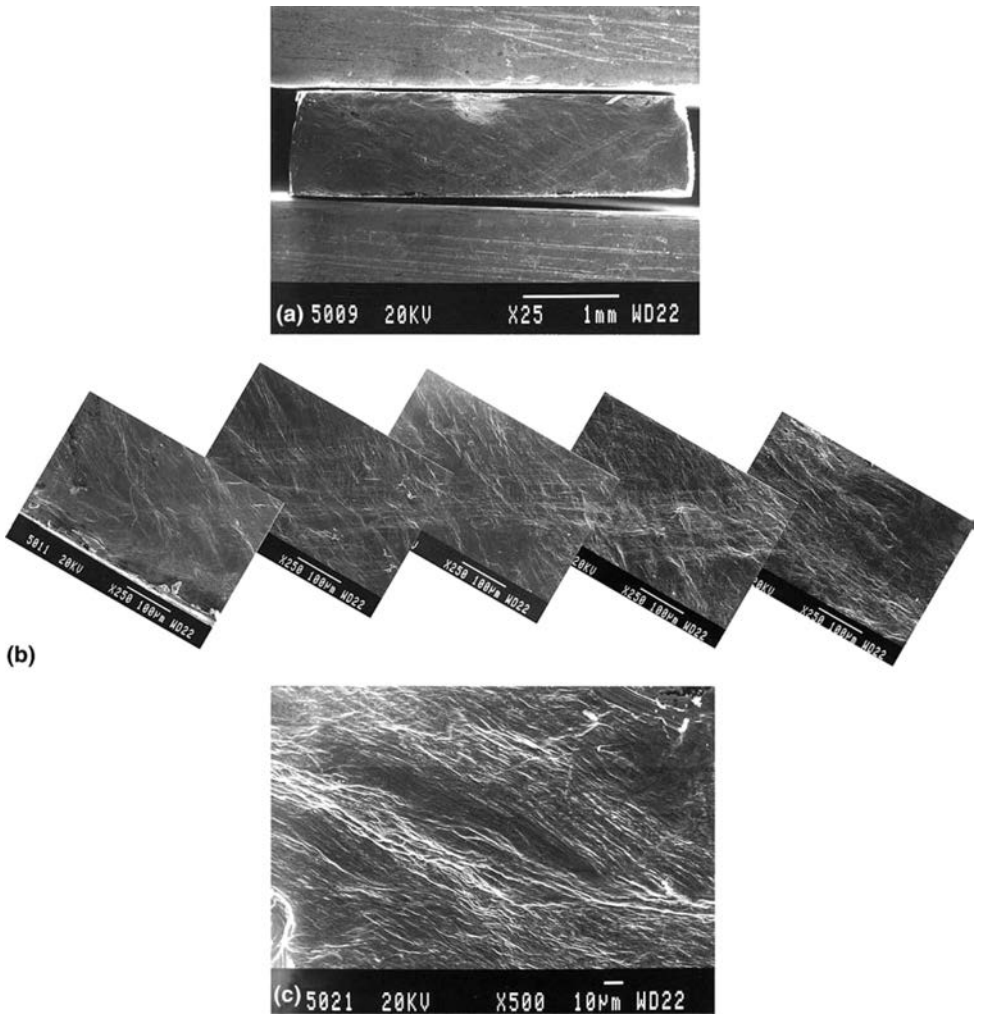

FIG. 27. SEM micrographs of the side face of a dynamically loaded ECAE Fe. a) Overall surface at a low magnification (loading is along the vertical direction and the sandwiched piece is the specimen); b) A collage showing the shear band contrast; c) An enlarged image showing the details of some shear bands. Note that in (b) the specimen has been rotated about 45° clockwise with respect to the loading direction to save space. The specimen was loaded to a true strain of ∼0.55 at a strain rate of ∼7000 s^{-1}, cf. WEI *et al.* [56].

rise. What is more, in Fig. 28d, a layer of wavy structure within the macroshear band can be seen, suggesting rotation and twisting of the material therein under dynamic loading.

Figure 29 shows the etched specimen, where the macroshear band is clearly revealed with a well-defined width of about 15 μm. The two white lines are added to identify better the macroshear band boundaries in the specimen.

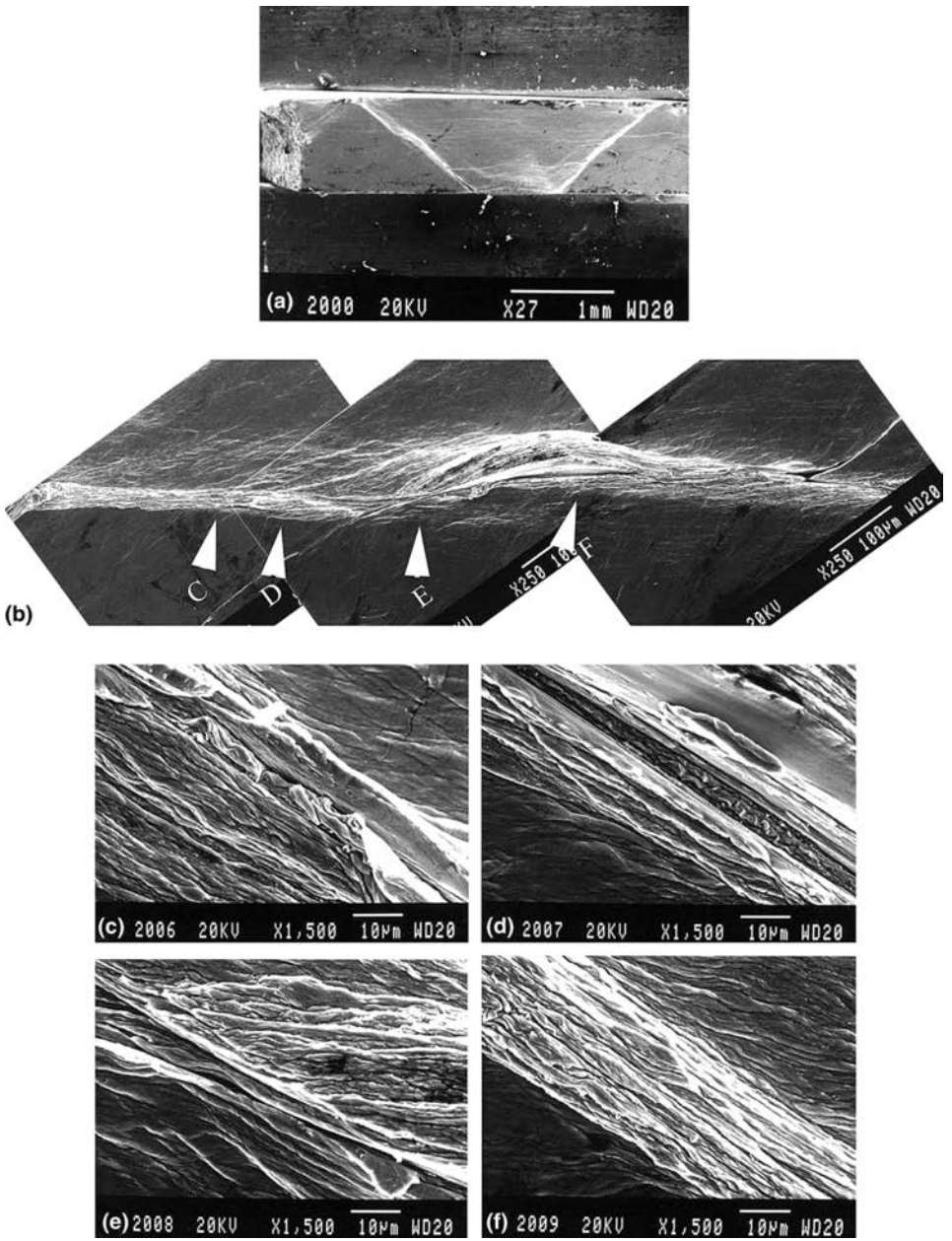

FIG. 28. A low magnification SEM micrograph (a) showing two major shear bands (loading is along the vertical direction, and the sandwiched piece is the specimen). Both the right and the left bands are oriented at an angle of ca. 45° relative to the loading direction. (b) Enlarged image of the left band in (a), with the details of the areas indicated by arrows given in (c)–(f). Note that in (b) the specimen has been rotated about 45° counter-clockwise with respect to the loading direction to save space. The specimen was loaded to a true strain of ∼0.6 at a strain rate of ∼8000 s^{-1}, cf. WEI *et al.* [56].

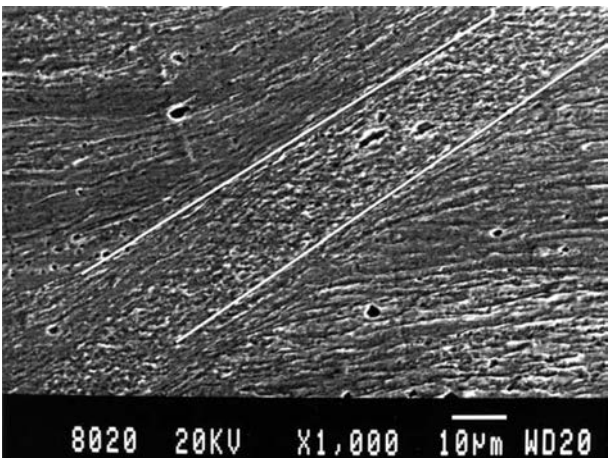

FIG. 29. Post-loading sample was polished and then etched using 5% Nital to reveal the microstructure, where the shear band is clearly seen with a width of about 15 μm. The boundaries of the adiabatic shear band have been marked out by a pair of white lines for the ease of identification, cf. WEI *et al.* [56].

CHENG *et al.* [4] observed the mode and evolution of the plastic deformation in nc-Cu. Their tensile tests were terminated before failure. The samples were unloaded, as shown for example at the end of the stress-strain curve of Fig. 30a. Figure 30b is a close view of the surface morphology for the sample unloaded right before the eventual failure, shoving a further development of the slanted macroshear zone. The shear offset on the sample edges is obvious. Signs of necking and off-axis banding become visible only in the large stage of plastic deformation. The macroshear zone contains numerous slip markings due to shear bands micrometers in width. At this point a crack begins to develop, causing the onset of load drop. Figure 30c displays the development of the macroshear localization as captured by a high-speed camera for a sample tested at 10^{-4} s^{-1}. The onset of plastic instability was found to be as early as around 3% of strain, whereas signs of necking appeared only much later (last three pictures).

Figure 31 shows an SEM micrograph of the fracture surface after tensile test. The image clearly indicates ductile fracture as characterized by the dimpled features.

JIA *et al.* [15] investigated deformation behaviour and plastic instabilities of ultrafine-grained titanium. Figure 32 shows a true stress-strain curve for the as-processed UFG-Ti, in comparison with that for the CG-Ti, obtained uniaxial compression at 2×10^{-4} s^{-1}. At a strain of 6% the flow stress of the UFG-Ti (1.02 GPa) is more than twice that of CG-Ti (0.45 GPa), consistent with the Hall-Patch relationship for conventional Ti. The as-processed UFG-Ti exhibits little strain hardening, with a nearly perfectly plastic behaviour at strain

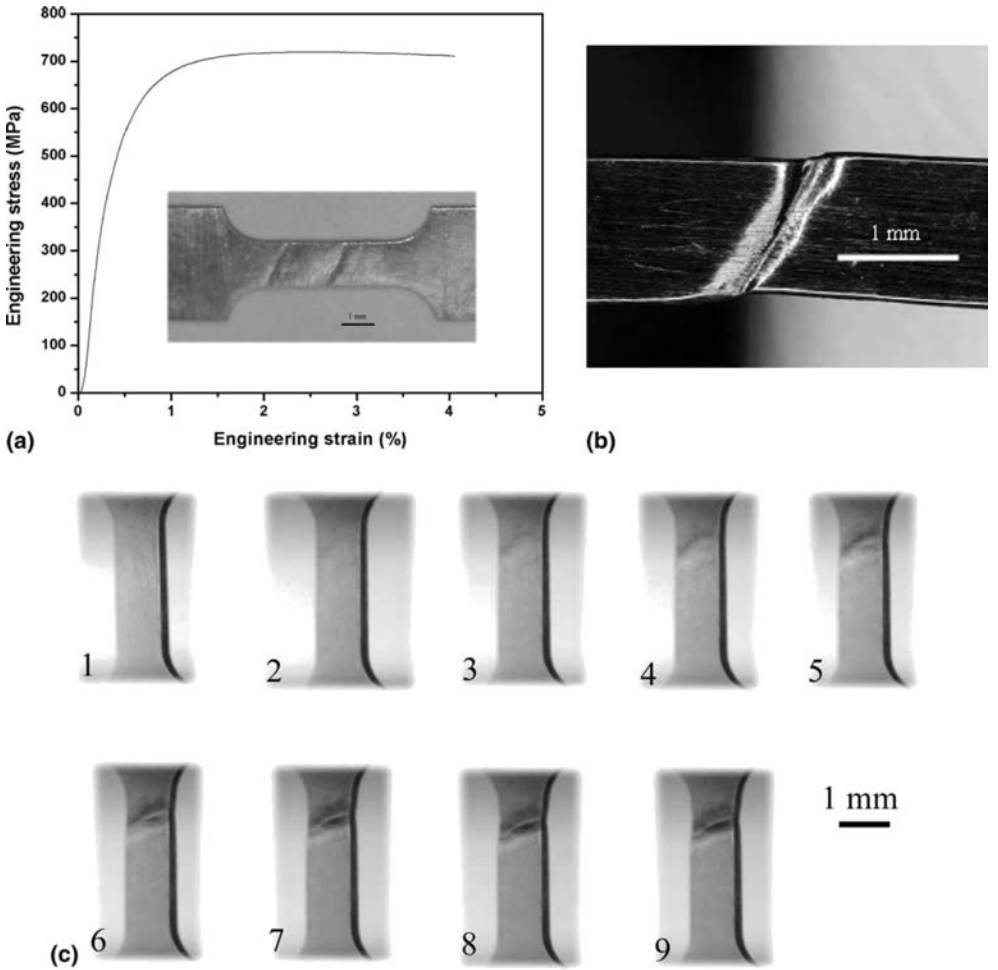

FIG. 30. (a) Tensile test, terminated before failure, of nc-Cu at RT, $\dot{\epsilon} = 10^{-4}$ s^{-1}. Shear location was observed. (b) An optical micrograph showing the shear zone and shear steps before cracking fails the sample. (c) The evolution of shear localization as captured by a high-speed camera. The corresponding engineering strain is as follows: (1) 0%; (2) ∼3.2%; (3) ∼3.9%; (4) ∼4.3%; and (5)–(9) were taken in the strain range of 4.6–7.0%. These pictures were captured from one sample that was tested at a strain rate 10^{-4} s^{-1}. The use of a high-speed camera avoids the smearing of images during strain. The samples were ball-milled at LN_2T for 3 h and RT for 5 h, cf. CHENG *et al.* [4].

above 5%. In comparison, CG-Ti shows obvious strain hardening. The stress-strain curve for UFG-Ti after annealing is also included in Fig. 32. Compared with the as-processed case, the yield strength of the annealed UFG-Ti is lower. The strain-hardening rate, on the other hand, is higher than the as-processed case for strains less than ∼5%, which is attributable to the recovery of the

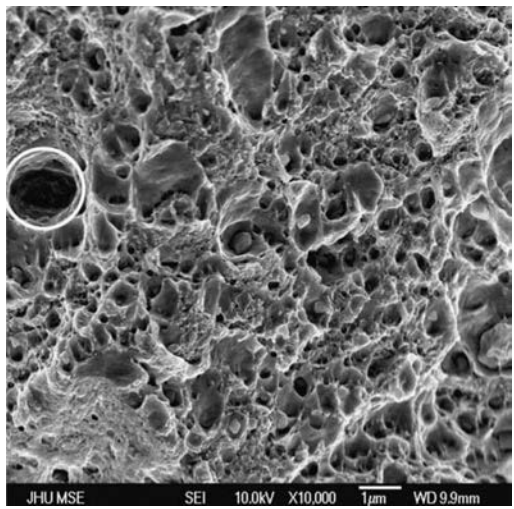

FIG. 31. Fracture surface of nc-Cu after tensile test to failure (cf. Fig. 3). The samples were ball milled at LN_2T for 3 h and RT for 5 h. The white circle shows a pore possibility left-over after consolidation, cf. CHENG *et al.* [4].

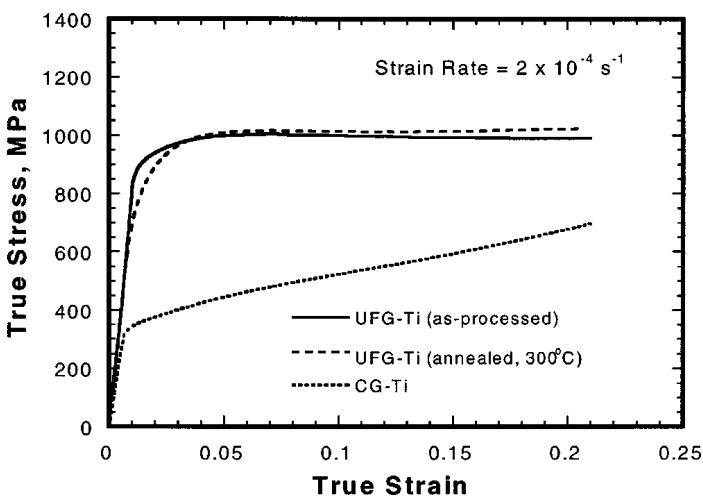

FIG. 32. Typical compressive true stress-strain curves for UFG-Ti (as processed and annealed) at a quasistatic-strain rate, with a curve for CG-Ti for comparison are shown, cf. JIA *et al.* [15].

cold-worked grains. However, due to the small grain size, the capacity for the accumulation of dislocations and twin boundaries and hence strain hardening, remains very limited and far less than that of CG-Ti. The higher strain hardening of the annealed UFG-Ti would also help to overcome softening caused by flaws or damage sites operative in tension. These predictions agree well with the

tension test curves (cf. Fig. 33a) and the necking morphology (cf. Fig. 33b), the authors have observed. The tensile fracture surface also shows clear ductile (cup and cone) features (cf. Fig. 33c), as expected from the large ductility seen in compression.

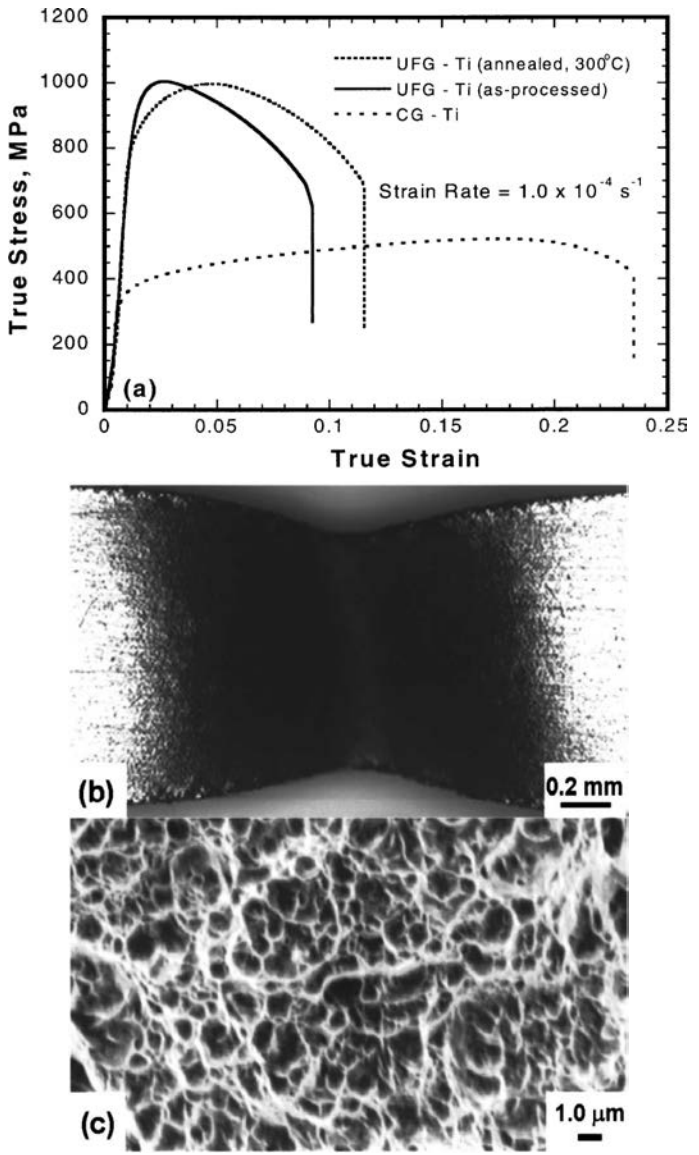

FIG. 33. (a) Tensile true stress-strain curves for as-processed and annealed UFG-Ti, in comparison with that of CG-Ti; (b) Optical micrograph showing necking in the annealed UFG-Ti; (c) Scanning electron microscopy of typical ductile features on the fracture surface of the sample in (b), cf. JIA *et al.* [15].

A typical true stress-strain curve for annealed UFG-Ti at a high-strain rate 4.3×10^3 s^{-1} is compared with a quasistatic curve in Fig. 34a, together with two corresponding curves for the CG-Ti at similar strain rates. The strain-rates dependence of the flow stress at a constant strain 6% is plotted in Fig. 34b for the strain-rate range from 2×10^{-4} to 9×10^{-4} s^{-1}. If a linear relationship is assumed, the UFG-Ti lines have similar slopes $(\partial\sigma/\partial\log\dot{\epsilon})_\epsilon$, indicating that he magnitude

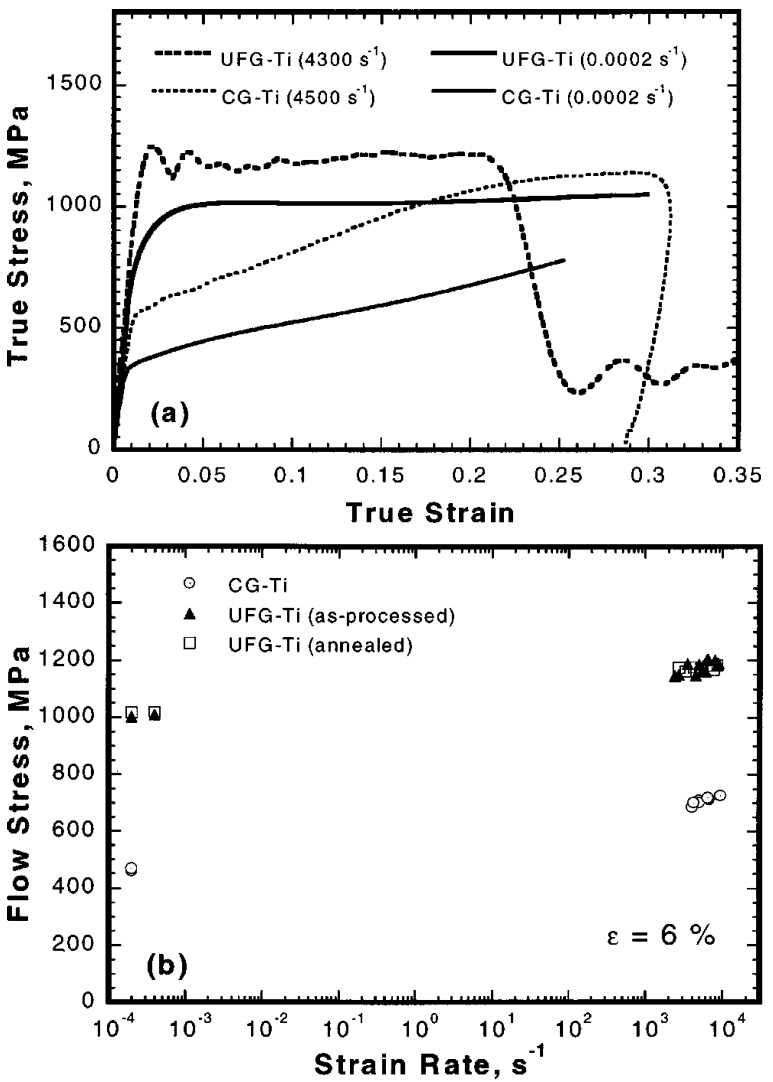

FIG. 34. (a) Comparison of high-strain-rate true stress-strain curves with those at quasistatic-strain rates for both the annealed UFG-Ti and CG-Ti are shown. (b) Strain-rate dependence of the flow stress of UFG-Ti and CG-Ti at a strain of 6% is presented, cf. JIA *et al.* [15].

of the strain-rate enhancement of the flow stress (∼200 MPa) is similar for these two very different grain sizes. However, due to the elevated strength of UFG-Ti, the strain-rate sensitivity, m, defined as $(\partial \log \sigma / \partial \log \dot{\epsilon})_\epsilon = \left(\frac{1}{\sigma}\right)(\partial \sigma / \partial \log \dot{\epsilon})_\epsilon$, drops by a factor of 2–3 relative to that for CG-Ti (from 0.025 to 0.009). The value of m affects the necking instability, the material with a higher value of m is more stable. Thus, the low m renders the UFG-Ti less resistant to necking, and contributes to the fast post-necking softening and reduced elongation to the failure observed in Fig. 33.

In the paper (cf. WANG *et al.* [51]) extended the mechanical testing of nanostructured Ti to much larger strains and a wide range of strain rates, in order to understand what factors and how they control the deformation/failure behaviour of UFG-Ti. They paid special attention to the possibility of twinning activities in nanostructured Ti that were previously overlooked. In order to do so, the mechanical properties of commercial purity of nanostructured titanium prepared by equal channel angular pressing plus cold rolling (grain size ∼260 nm) were systematically characterized. Hexagonal close-packed (*hcp*) ultrafine-grained (UFG) titatnium processed by sever plastic deformation (SPD) has gained wide interest due to its excellent mechanical properties and potential applications as biomedical implants.

It is well-established that deformation twinning is an important mode of deformation in coarse-grained (CG) *hcp* materials. Experimental observations confirmed that the nanostructured titanium prepared by SPD contains not only high densities of dislocations but also a significant amount of deformation twins. Such unique microstructural characteristic suggests that the deformation mechanism and failure mode of nanostructured Ti may be different from those of other UFG materials.

Figure 35 shows true stress-strain curves of UFG-Ti with the strain rate in the range of 10^{-4} s^{-1} – 10^{-1} s^{-1}. For comparison, the stress-strain curve of a CG-Ti is also included. A considerably elevated strength was observed in UFG-Ti with the yield stress 3–4 times higher than that of CG-Ti. In terms of ductility, UFG-Ti fails after a total compressive strain of ∼30%, as compared to ∼60% in CG-Ti. Careful examinations of the strain hardening behaviour in UFG-Ti and CG-Ti reveal distinctive differences. The CG-Ti demonstrates a strong strain hardening behaviour throughout the test. Such an increasing strain hardening behaviour in CG-Ti is believed to be associated with extensive twinning. In contrast, a different scenario is observed for the plastic flow of UFG-Ti, which exhibits initially strain hardening, with a near perfectly plastic behaviour at strain up to 15%. This is strain hardening behaviour at small strain agrees with previous observations (cf. JIA *et al.* [15]) and is believed to render tensile instability in nanostructured Ti. At large strains, however, a non-negligible strain hardening

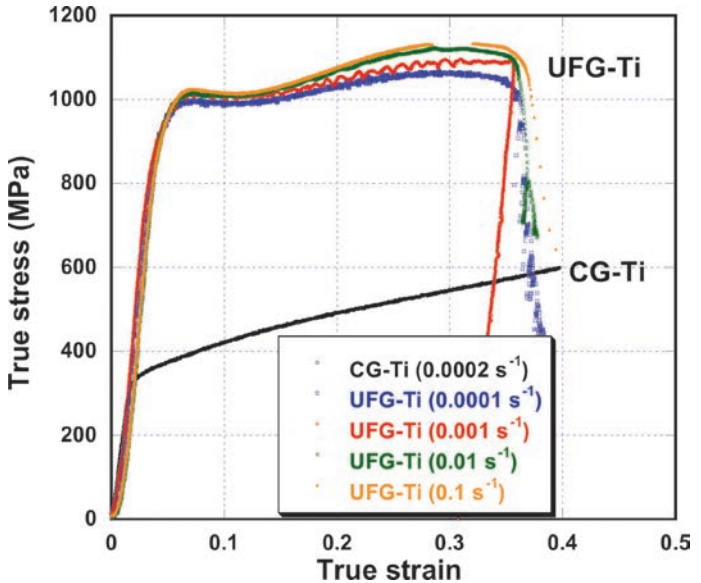

FIG. 35. Room temperature compressive true stress-strain curves of nanostructured Ti and the coarse-grained Ti over strain rate range of 10^{-4} s^{-1}–10^{-1} s^{-1}, cf. WANG *et al.* [51].

is observed. The strain hardening for UFG-Ti becomes more pronounced when the samples were tested at high strain rates, as shown in Fig. 36.

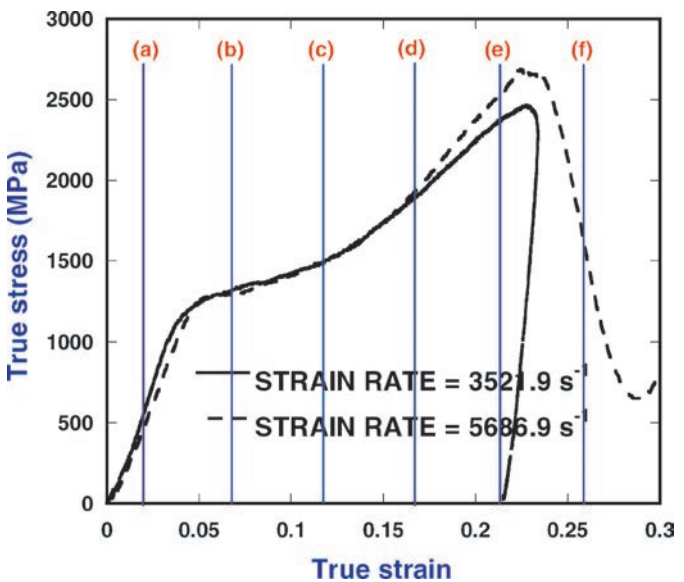

FIG. 36. Dynamic compressive true stress-strain curves of nanostructured Ti at room temperature, cf. WANG *et al.* [51].

Figure 37 displayed sequential TEM bright field images of the as-processed and deformed UFG-Ti. Due to the cold-rolling procedure, many grains in the as-prepared samples exhibit filamentary shape along the longitudinal rolling direction (Fig. 37a), with an average grain size of ∼260 nm. Dislocation cells and

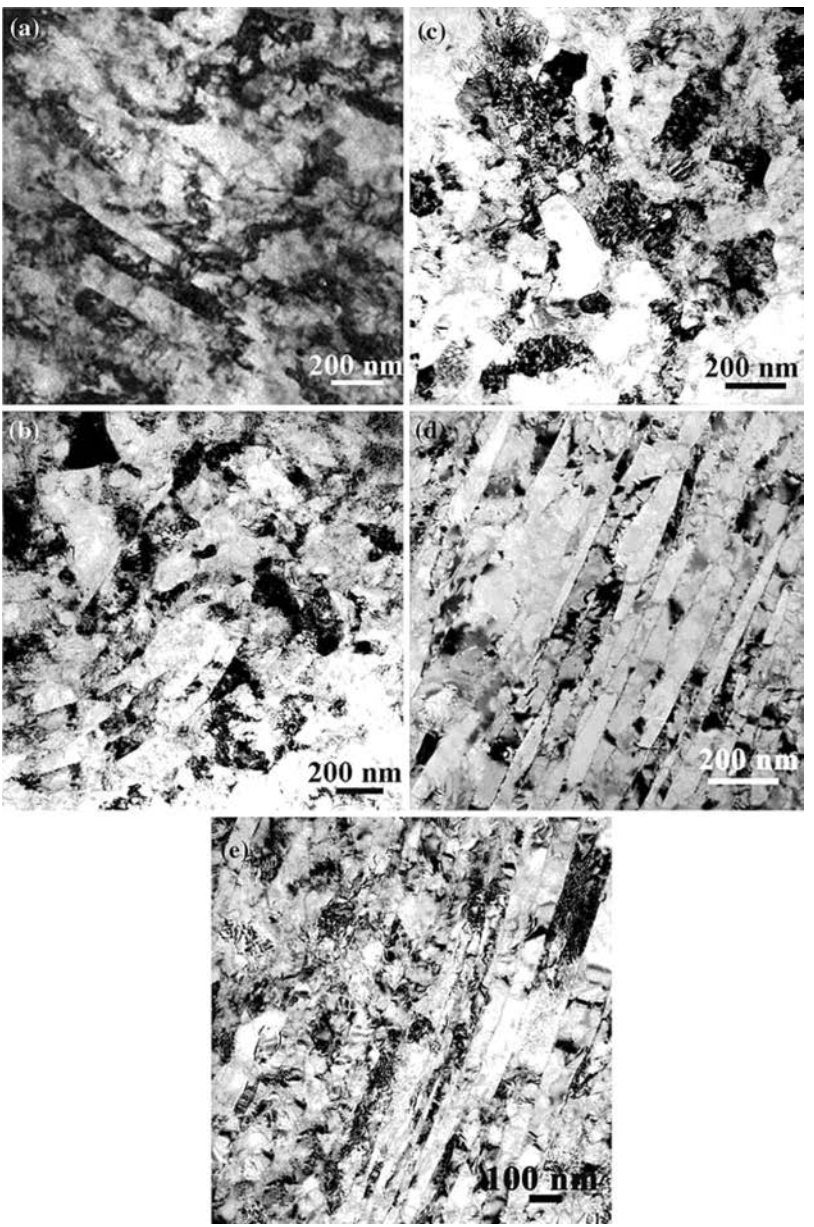

FIG. 37. TEM bright-field images of a) as-processed, b) 8%, c) 30%, d) high strain rate, and e) low-temperature (77 K) deformed UFG-Ti, cf. WANG *et al.* [51].

extremely high density of dislocations are the typical microstructural features. Deformation twins resulting from severe plastic deformation are also visible inside grains with the twin band width of the order of ∼150 nm. After 10% deformation (Fig. 37b), the ultra-fine-grains become more or less equiaxed, though some grains with straight boundaries and elongated contours are still observable. The average grain size remains approximate constant across the transverse direction. After 30% strain (Fig. 37c), the grains look completely equi-axed (the sample failed at this point). The transformation of grain shape from fibrous type to equi-axial type during the quasi-static compressions implies the change of grain orientations and evolution of the texture, suggesting that the dislocation slip plays a significant role during plastic deformation of UFG-Ti.

TEM examinations in quasi-static deformed samples supports the notion that dislocation slip is the major deformation in nanostructured Ti at slow deformation and room temperature (cf. Zhu *et al.* [62]).

At dynamic loading rates (10^3–10^4 s^{-1}), however, a different scenario is observed (Fig. 37d). Deformation twin with the band width in the range of 50–100 nm becomes the characteristic microstructural feature. The twin bands in as-processed samples are noticeably wider, suggesting that deformation twinning has become an important event of the high strain rate deformation of UFG-Ti.

Extensive twinning activities were also observed when nanostructured Ti was deformed at cryogenic temperature (77 K), as shown in Fig. 37e, cf. Wang *et al.* [52]. The twin bands observed in low-temperature deformation is narrower (in the range of 10–50 nm) than those seen at high strain rates. This indicates that the twinning activity in nanostructured Ti is closely tied to deformation conditions such as strain rates and temperature.

The strain hardening behaviour has direct influence on the failure mode of UFG-Ti. The development crack during dynamic testing was captured by a high-speed camera in Fig. 38. The alphabetic order of the pictures is the same as those marked on the stress-strain curve of UFG-Ti (Fig. 36), with each letter representing a different strain level. The time interval between two frames is 10 ms, and the camera exposure time for each image is 1 ms. The cracks started to develop in the late stage of deformation (Fig. 36f) where the substantial strain softening has advanced.

In two papers (cf. Wei *et al.* [55] and Wei *et al.* [57]), the authors investigated the quasi-static and dynamic mechanical behaviour (especially dynamic failure) of ultra-fine grained tungsten (UFG W) under uniaxial compression. They used sever plastic deformation (SPD) to refine the microstructure of conventional W with commercial impurity levels. The microstructure was analyzed using TEM, cf. Fig. 39. The UFG W was tested at both quasi-static loading rates (10^{-4}–10^0 s^{-1}) and dynamic loading rates ($\sim 10^3$ s^{-1}) using a compression Kolsky bar, cf. Fig. 40.

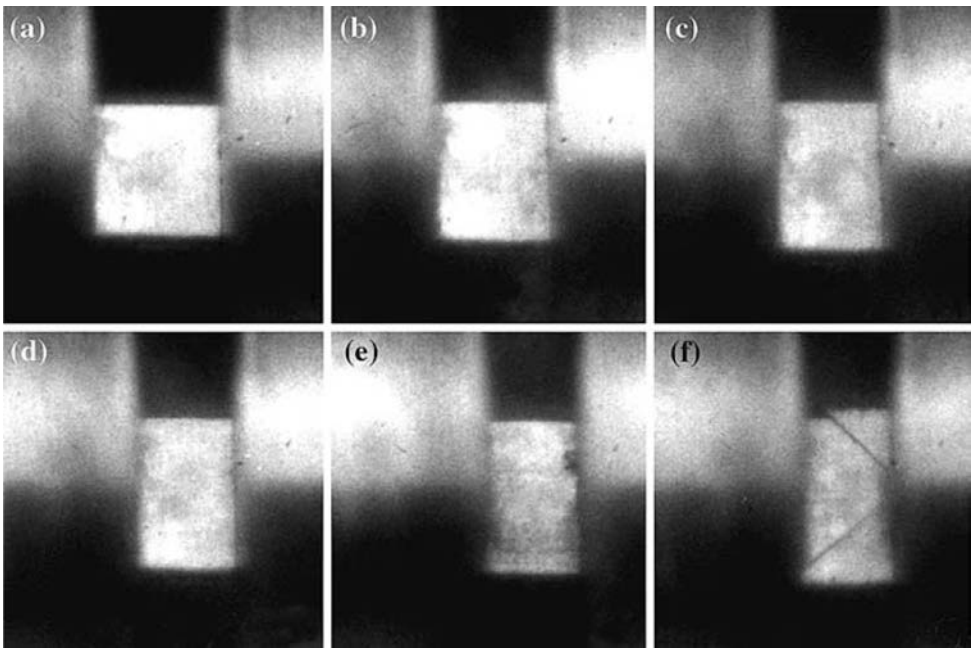

FIG. 38. (a)–(f) *In situ* high speed camera pictures of UFG-Ti during a dynamic compression test. Note the development of cracks with Increasing strains, cf. WANG *et al.* [51].

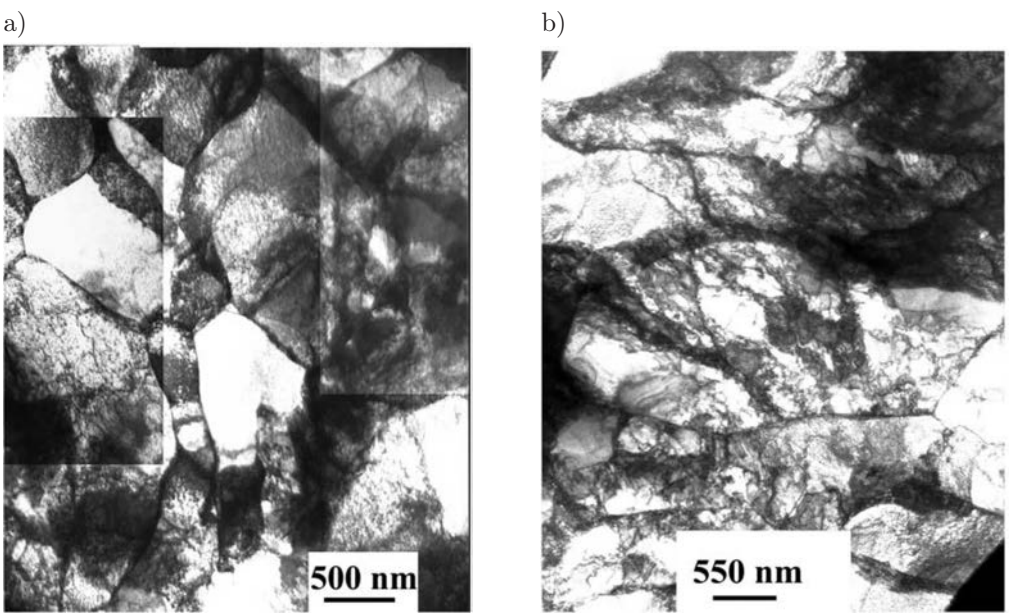

FIG. 39. Transmission electron micrographs of SPD-processed (ECAP + rolling) UFG W (a, b), showing grains and dislocation cell structures refined to sizes of the order of 500 nm, cf. WEI *et al.* [55].

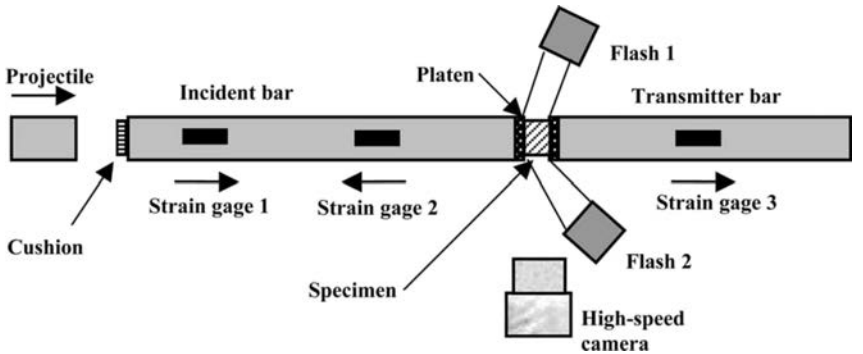

FIG. 40. Schematic of experimental setup for Kolsky bar compressive test with a high-speed camera synchronized with the system. Strain gages 1, 2, 3 are used for the high-speed camera, the incident/reflected and transmitted waves, respectively. The platens are a set of impedance-matched tungsten carbide disks collared with Ti-6Al-4V for the protection of the bars, cf. WEI *et al.* [55].

Figure 41 displays the stress-strain curves under various strain rates (from quasi-static to dynamic) for the ECAP W and W, that was processed by ECAP

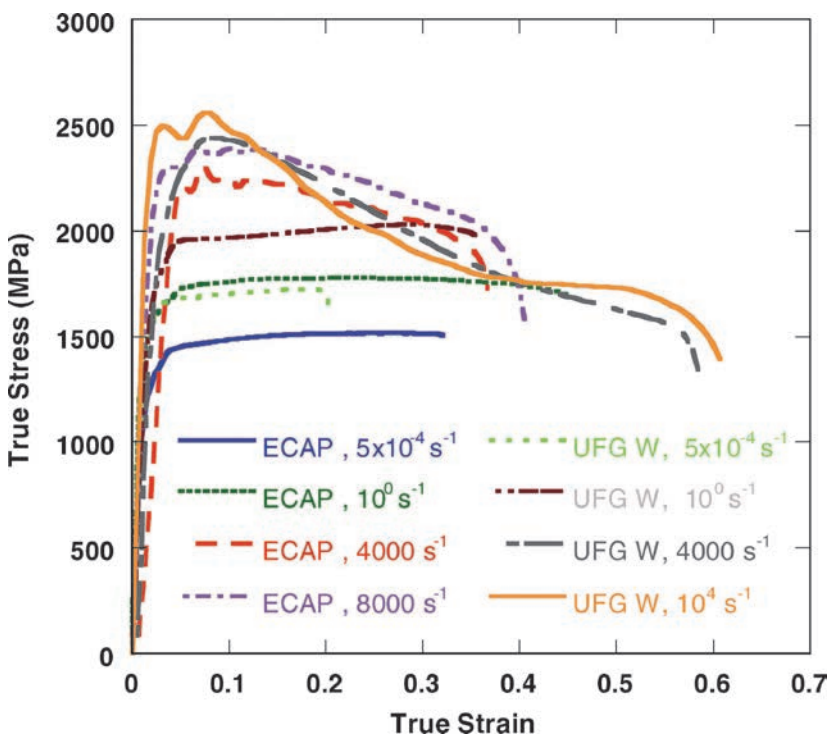

FIG. 41. True stress-strain curves of the ECAP W and the ECAP+CR (UFG) W, under uni-axial quasi-static, and dynamic (Kolsky bar) compressive loading, cf. WEI *et al.* [55].

at 1000°C followed by cold-rolling (referred to hereafter as ECAP+CR W). ECAP at 1000°C (six passes in this case) has elevated the quasi-static flow stress to ∼1.5 times that of the CGW. ECAP has also markedly reduced the strain hardening. Cold rolling further strengthens the material until the flow stress is nearly doubled compared to the CGW. Under dynamic loading, both the ECAP W and ECAP+CR W exhibit flow softening after small plastic strains, in contrast to the dynamic behaviour of CGW where slight work-hardening is observed. This flow softening is in part due to the accumulation of plastic work that is converted into heat during dynamic loading.

Due to combination of high strength and ductility and the reduced role of stabilizing mechanisms (strain hardening and strain rate hardening), the UFG *bcc* microstructure will have an unprecedented low resistance to softening mechanisms. Plastic flow will be more likely to localize in zones and bands, in which very high strains and strain rates are concentrated. This was indeed observed upon uniaxial high-rate compressive loading of the high-strength UFG-W.

Figure 42a shows an optical micrograph of the UFG-W after loading at a strain rate of 7500 s^{-1}. Two major shear zones, at an angle of approximately 45° relative to the loading direction, are clearly observed. A scanning electron image of a side face, with marked shear zones, is shown in Fig. 42b. Figure 42c shows clearly evidence for the closely bundled flow lines as well as the subsequent incipient fracture along the localized adiabatic shearing.

To investigate the dynamics of the shear banding process and its relation with other phenomena, a high-speed camera was synchronized with the Kolsky bar system. *In situ* high-speed photography shows the evolution of the adiabatic shear band and subsequent fracture of the specimen. Figure 43 displays the corresponding stress-time and stress-strain curves from one such experiment (cf. Figs. 43a and 43b) and show two frames taken at the time or the strain indicated by the square symbols on the curves (cf. Figs. 43C and 43I). The first frame (cf. Fig. 43C) was taken before the plastic deformation occurred. Latter frame (cf. Fig. 43I) shows the well-developed shear bands. The authors pointed out that both post-mortem microscopic observations and in-situ high-speed photography reveal intensive plastic shear localization in the UFG-W, and the letter indicates that the shear localization takes place at a very small strain level. Fracture has also been observed as a consequence of the sever adiabatic shear localization in the UFG-W.

It is important to stress that materials with high flow stress, high thermal sensitivity, small strain hardening and small strain-rate sensitivity are more susceptible to adiabatic shear band localization under dynamic compression.

Thus, it is very important to investigate strain rate sensitivity for UFG-W. Figure 44a displays double-log plots for W with different microstructure (grain

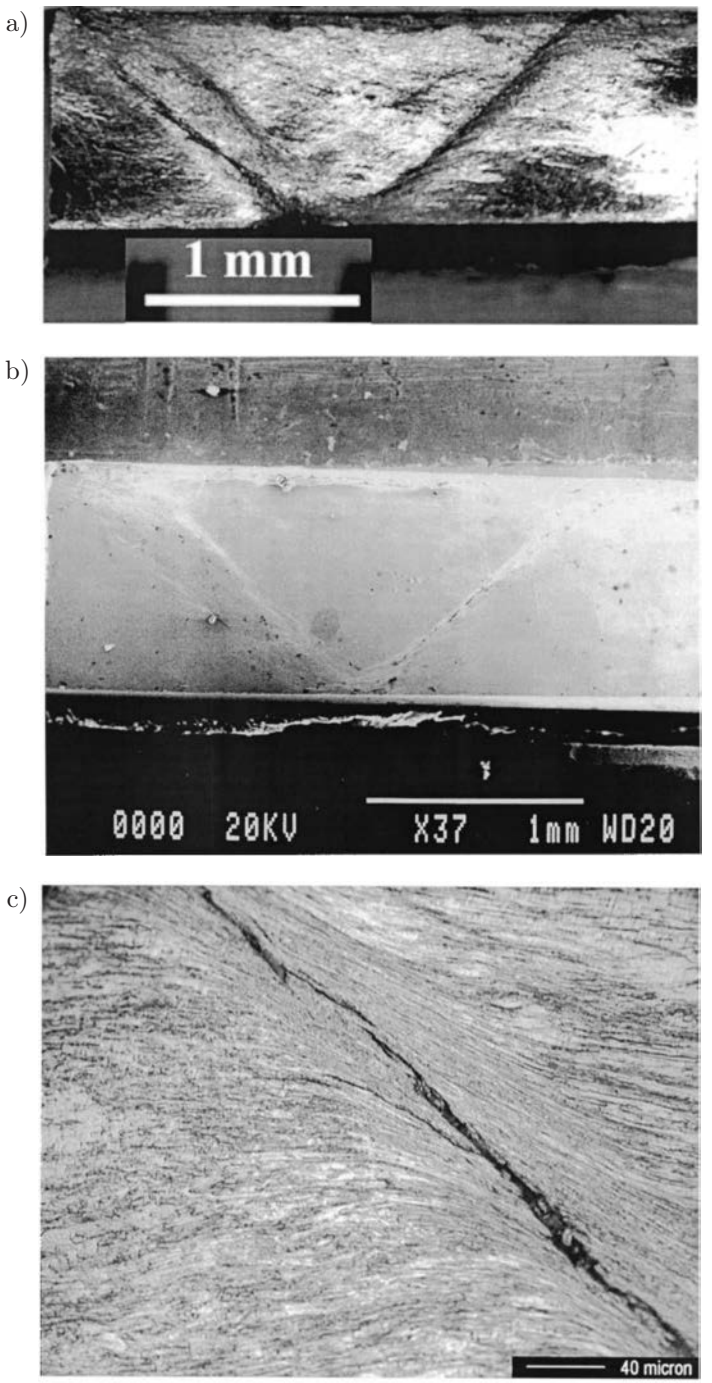

FIG. 42. (a) Optical and (b) scanning electron microscope images showing the shear zones, and (c) the intense concentrated plastic flow with crack initiation inside the shear zone, cf. WEI *et al.* [55].

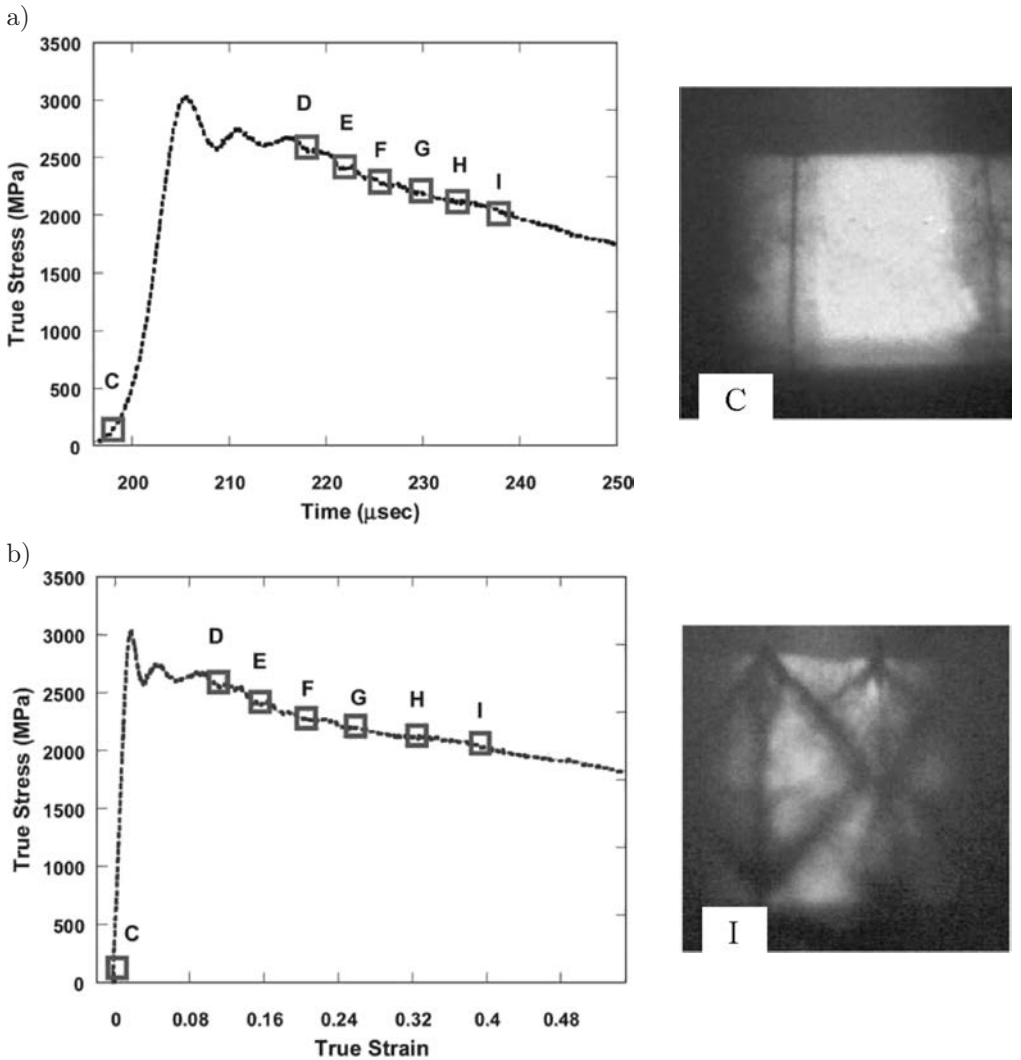

FIG. 43. The stress-time curve (a) and stress-strain curve (b) for a uniaxial compression Kolsky bar test of an SPD UFG W. The square boxes in each figure indicate the time or strain level at which each frame was captured, cf. WEI *et al.* [55].

sizes), showing that the strain rate sensitivity of UFG-W has been cut to half the value of the CG-W (the CG-W of commercial purity has an m of $\sim$0.04). Figure 44b includes previous results on *bcc* Fe, Ta and V showing that m can drop substantially when grain size is refined.

Microstructure and mechanical properties of super-strong nanocrystalline tungsten processed by high-pressure torsion have been recently investigated by WEI *et al.* [58].

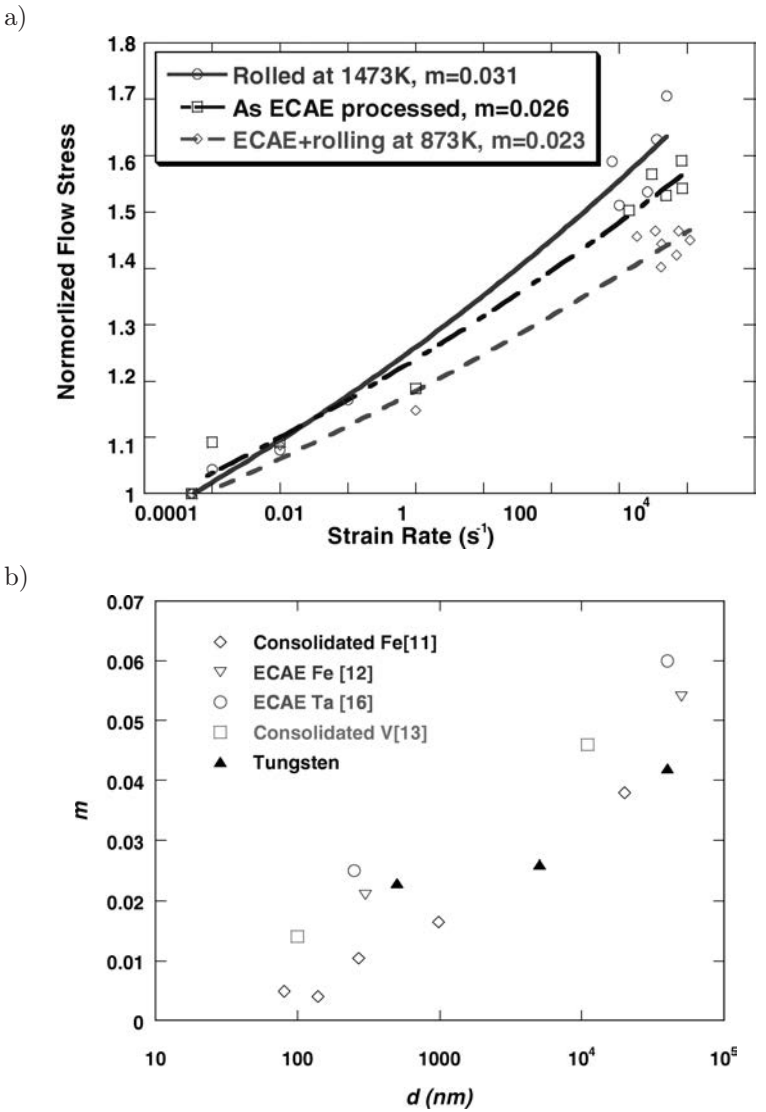

FIG. 44. (a) Flow stress-strain rate curves of W after working under various conditions. The CG W of commercial purity has an m of $\sim$0.04 from an early investigation. (b) Strain rate sensitivity, m, is reduced monotonically with microstructure refinement into the UFG regime, in several *bcc* (Fe, Ta, V) metals (open symbols), cf. WEI *et al.* [55].

2.6. Yield strength reduction due to dynamic grain growth

During prolonged mechanical test, or for samples that have very high purity, the high strength may degrade with time. This is due to the large excess energy associated with grain boundaries in nc materials, which is expected to cause

instability in their nc grain size distributions. Evolution towards equilibrium can be driven, or promoted, by stress during deformation process.

Indeed, recent studies have found that indentation induced rapid grain growth in nc Cu and nc Al.

After these initial observations of indentation-induced grain growth in nc Cu and nc Al, grain growth was observed experimentally in nc materials that are deformed under other deformation modes.

Surprisingly, it is found that grain coarsening is even faster at cryogenic temperatures than that at room temperature, cf. Dao *et al.* [7].

2.7. Strain induced anisotropy effects

Grain refinement has long been the matter under investigation to improve fatigue and fracture resistance of engineering materials and alloys. It is of great interest to study the effects of grain refinement on fatigue behaviour at the nanoscale range when average, as well as peak, grain sizes are below 100 nm, cf. Dao *et al.* [7].

Recent experimental observation on the fatigue life and fatigue crack growth for full-density nc metals, using electrodeposited nc Ni (with an average grain size in the range 20–40 nm, and peak grain size near 70 nm), Hanlon *et al.* [12] showed the effect of grain size on the fatigue resistance. Nanocrystalline Ni was shown to have a moderately higher endurance limit when subject to stress-controlled fatigue loading than ufc Ni, while both nc Ni and ufc Ni showed significantly higher fatigue resistance than the mc Ni. Experimental observations performed by Hanlon *et al.* [13] confirmed that over a wide range of load ratios, the nc Ni showed significantly lower resistance to fatigue crack growth.

Figure 45 shows SEM crack growth images of mc, ufc and nc Ni subjected to fatigue loading at 10 Hz and loading ratio $R = 0.3$. The crack path is much less tortuous with a decreasing grain size.

With the enhanced fatigue limit for nc metals but at the reduced crack growth resistance, it is likely that a controlled grain size gradient may bring benefit fatigue properties while avoiding unwanted disadvantages, cf. Dao *et al.* [7].

The behaviour of nanocrystalline metals under cyclic loading processes can be described properly when we take into account the residual stresses in a material, which have very important influence on the evolution of intrinsic nanostructure of metals.

The intrinsic nanostructure of nanocrystalline metals during loading, unloading and reloading processes can be changed very intensively. This change during load, unload, reload test for cryo-rolled nc Cu has shown by Wang and Ma [52], cf. Fig. 20.

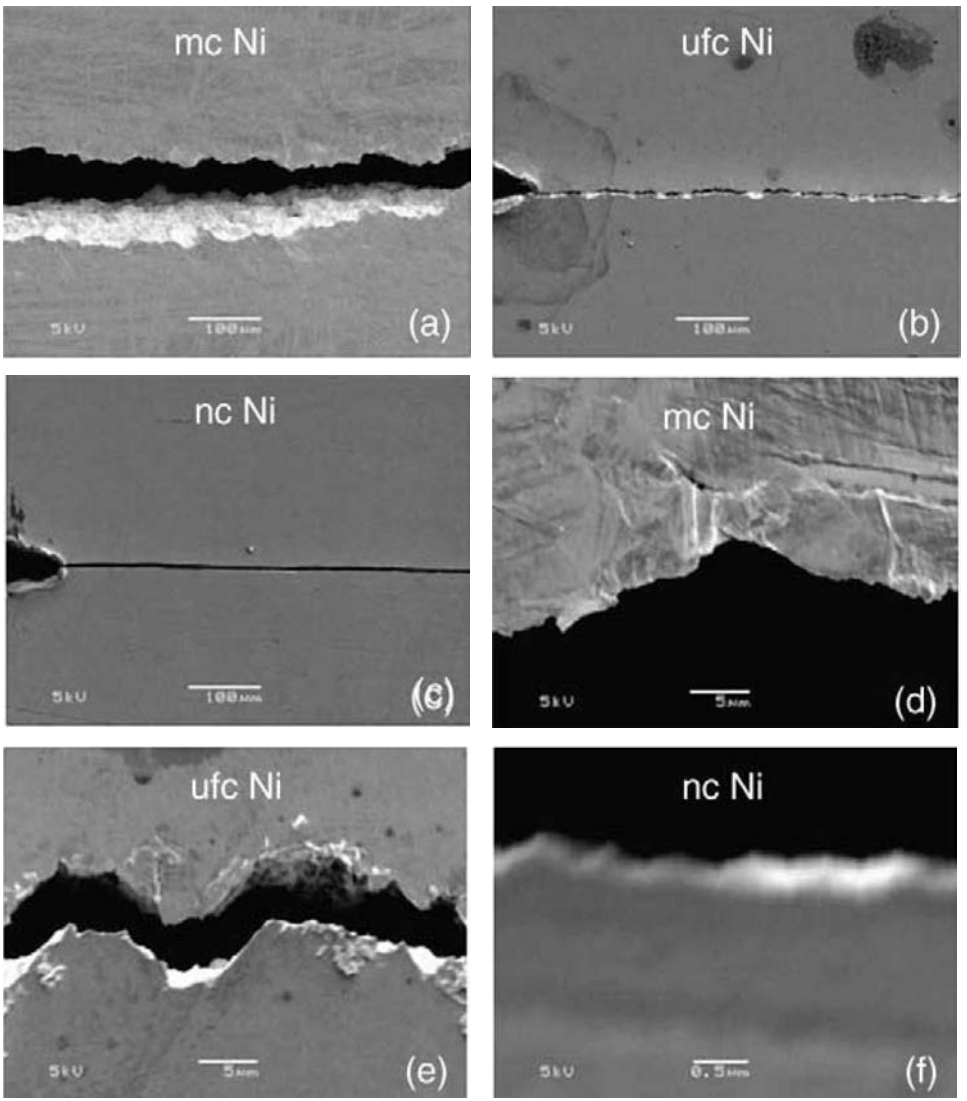

FIG. 45. Scanning electron micrographs of mc, ufc and nc Ni subjected to sinusoidal fatigue loading at the initial stress intensity factor values of 10, 6.2, and 8.5 MPa $m^{1/2}$, respectively. A cyclic frequency of 10 Hz and loading ratio $R = 0.3$ were used in all cases. Crack path tortuosity clearly decreases with grain refinement. Images (d)–(f) are high-magnification images of (a)–(c), respectively, and the magnification of (f) is 10 times of (d) and (e), cf. HANLON *et al.* [13].

2.8. Ductility and fracture

For many nanocrystalline metals, low ductility and premature fracture, sometimes the failure occurring even in the elastic range, were due to processing flaws

and artifacts, cf. Dao *et al.* [7]. However, nanocrystalline metals are characterized by a low work-hardening rate, which is a direct consequence of the low density of dislocation encountered after plastic deformation. This low work-hardening rate leads to tensile instability and a low tensile ductility. There are reports, recently published on increased ductility in nanocrystalline metals; very good example of this is the experimental investigation work by Cheng *et al.* [4] *in situ* consolidated nanocrystalline Cu. The authors reported on a much improved combination of tensile strength and ductility, over the tensile properties of other nc-Cu materials documented in the literature, cf. Fig. 46.

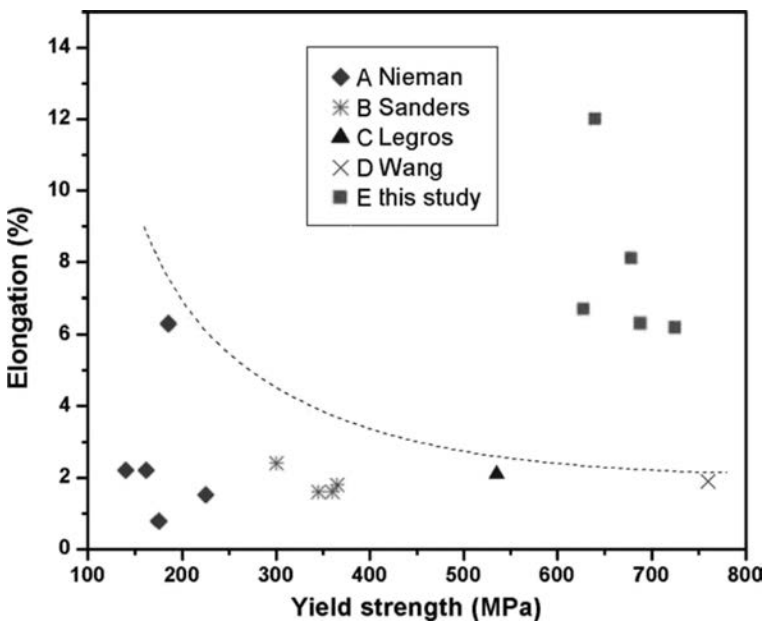

Fig. 46. Comparison of tensile yield strength and elongation to failure of various truly nc-Cu (average $d < 100$ nm) in literature. The dashed line shows a general trend as guide to the eye, cf. Cheng *et al.* [4].

The authors suggested that in most of the previous tensile tests, the nc-Cu used suffered from sample flaw problems. Flaws possibly accelerated the onset of cracking in the local regions with concentrated strains (shear band zones or necked regions). Although residual defects (porosity, microcracks) may still be present *in situ* consolidated nc-Cu, they are such a low population that tensile flow can be maintained to appreciable strain levels before cracking finally fails the sample, cf. Fig. 30. It is, therefore, conceivable that in samples without any residual porosity, an even larger tensile elongation could be achievable.

Fracture in nanocrystalline metals is a complex phenomenon of initiation, propagation and coalescence of micro(nano)voids or micro(nano)cracks, leading

to the separation of a body into two or more parts. The spacing/size of dimples, however for nanocrystalline metals, is considerably larger than the grain size on their specimens. KUMAR *et al.* [19] presented the interpretation of the evolution of micro(nano)cracks, cf. Fig. 47. The mechanisms responsible for void initiation are: (i) existing voids at grain boundaries and triple points; (ii) voids created by dislocation emission from grain boundaries; (iii) voids created by grain-boundary sliding which leaves wedges at triple junction; (iv) cavities created by the action of grain-boundary sliding on the ledges. The spacing of these initiation sites, which is larger than the grain size, determines the dimple size, cf. Fig. 48 and Fig. 31.

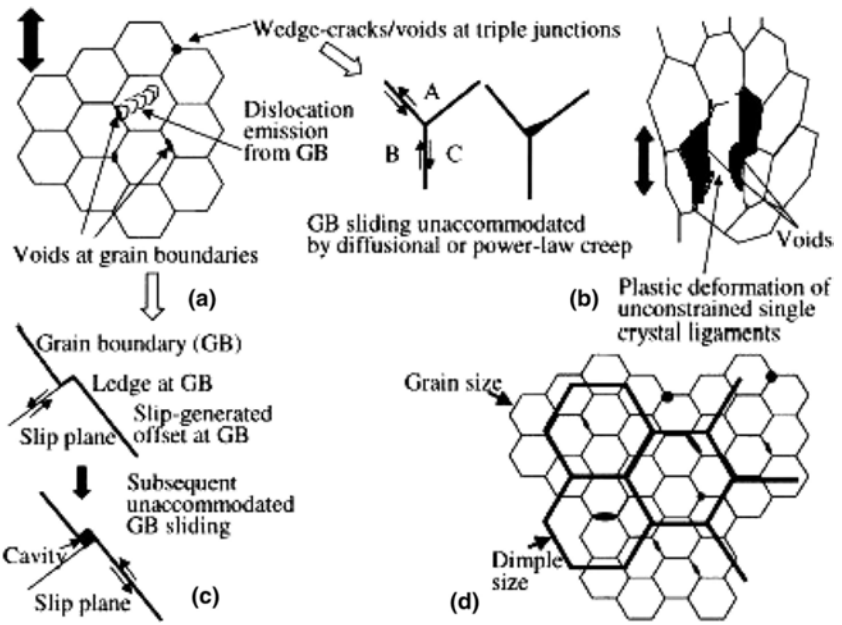

FIG. 47. Schematic illustration showing how deformation evolves in the nanocrystalline nickel and leads to (a) dislocation emission from grain boundaries, void formation/growth at grain boundaries and triple junctions, grain-boundary sliding; (b) the formation of partially unconstrained ligaments that deform plastically; (c) generation of cavities at grain-boundary ledges and (d) the interaction of these various features to produce final dimple size, KUMAR *et al.* [19].

Recent experimental observations have shown the interesting possibility, that nanosized grains rotate during plastic deformation and can coalescence along the directions of shear, creating larger paths for dislocation movement. As plastic deformation takes place, two neighboring grains might rotate in a fashion that brings their orientation closer together. This leads to the elimination of the barrier presented by the boundary between them, providing a path for more

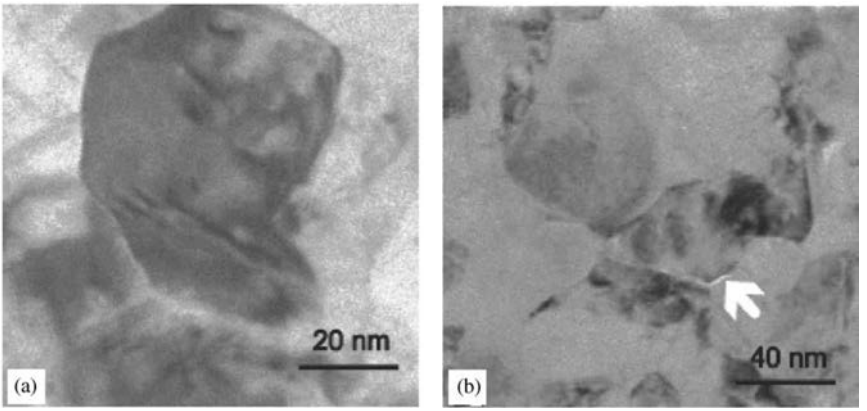

FIG. 48. Microstructure of nc-Ni after 4% plastic strain in compression: a) bright-field TEM image showing a few dislocations within a grain; b) a possible crack at a grain-boundary triple junction, WEI and ANAND [59].

extended dislocation motion. This mechanism can actually lead to softening and localization, and is consistent with the limited ductility often exhibited by nanocrystalline metals, cf. Fig. 49. The mechanism of rotation of neighboring nanograins and creation of elongated grains by annihilation of grain boundary during intensive plastic deformation within the localized region of macroshear band in consolidated nc-Fe, has been observed experimentally, cf. Fig. 26a.

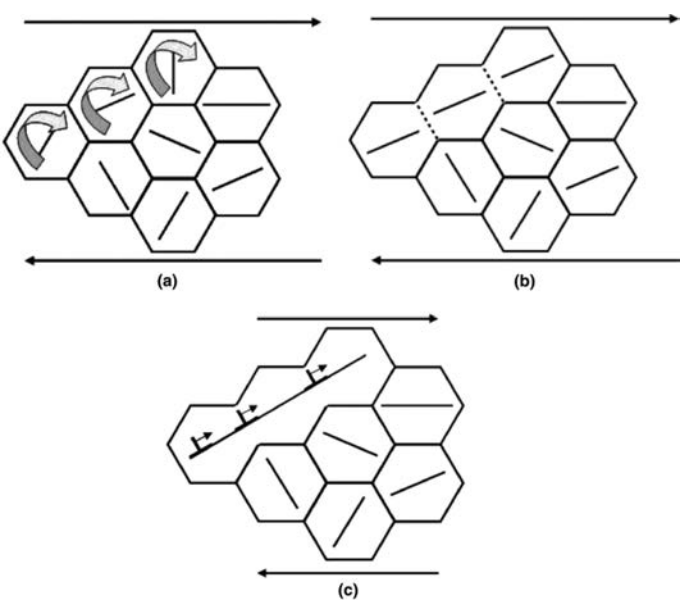

FIG. 49. Rotation of neighboring nanograins during plastic deformation and creation of elongated grains by annihilation of grain boundary, cf. MEYERS *et al.* [24].

3. Physical foundations

The rate and temperature dependence of the flow stress of metal crystals can be explained by various physical mechanisms of dislocation motion. The microscopic processes combine in different ways to give several group of deformation mechanisms, each of which can be limited to the particular range of temperature and strain rate changes.

The principal short-range barrier, the Peierls-Nabarro stress, is important for ultrafine crystalline *bcc* metals, whereas in ultrafine crystalline *fcc* and *hcp* metals, forest dislocations are the primary short-range barriers at lower temperatures, cf. Dao *et al.* [7] and Meyers *et al.* [24]).

Schematic representations of these two mechanisms in which the obstacles are overcome are given in Fig. 50. In each case, thermal fluctuations assist the applied stress in getting a dislocation segment L past the barrier. Both of these mechanisms lead to viscoplastic response of the crystal.

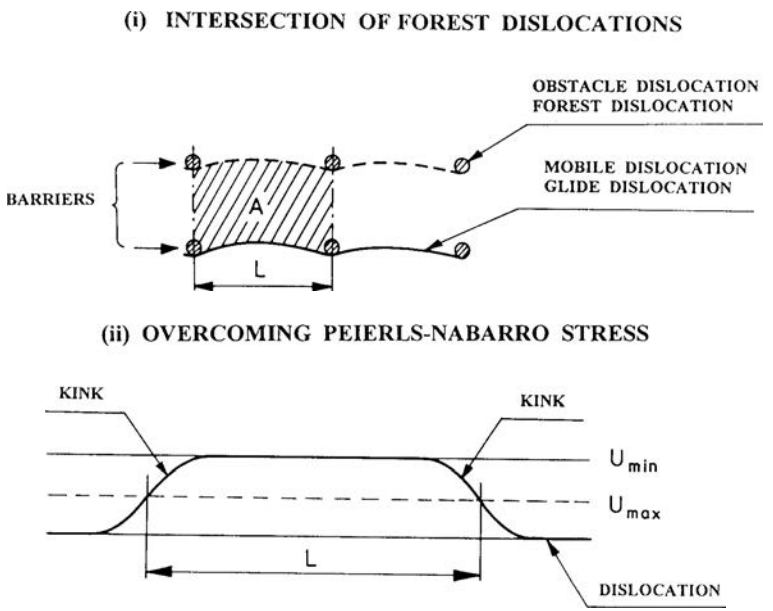

Fig. 50. Schematic representations of the physical mechanisms responsible for inelastic flow of *fcc*, *bcc* and *hcp* nc metals.

The main idea of the viscoplastic flow mechanism is to accomplish in one model the description of behaviour of single crystals valid for the entire range of strain rate changes. In other words, the main concept is to encompass the interaction of the thermally activated and phonon damping mechanisms, cf. Perzyna [28–32].

To achieve this aim, the empirical overstress function Φ has been introduced and the plastic strain rate is postulated in the form as follows (cf. PERZYNA [41])

$$\dot{\epsilon}^p = \frac{1}{T}\left\langle \Phi\left[\frac{\tau}{\tau_Y(\epsilon^p,\vartheta,\boldsymbol{\mu}^*,d)}-1\right]\right\rangle \operatorname{sgn}\tau, \tag{3.1}$$

where T is the relaxation time, $\langle\cdot\rangle$ denotes the Macauley bracket, τ is the actual stress and τ_Y is the yield stress function, which may depend on the inelastic strain ϵ^p, temperature ϑ and the internal state variables $\boldsymbol{\mu}^*$ and d (d is the average grain size). The internal state variable vector $\boldsymbol{\mu}^*$ may represent the density of obstacle dislocations, the density of mobile dislocations and the concentration of point defects.

We can use the Hall-Petch relation (2.2), then

$$\tau_Y = \tau_0(\epsilon^p,\vartheta,\boldsymbol{\mu}^*) + kd^{-n}, \tag{3.2}$$

where k is a constant and $0.3 \leq n \leq 0.7$.

Finally we have the constitutive assumption in the form

$$\dot{\epsilon}^p = \frac{1}{T}\left\langle \Phi\left[\frac{\tau}{\tau_0(\epsilon^p,\vartheta,\boldsymbol{\mu}^*)+kd^{-n}}-1\right]\right\rangle \operatorname{sgn}\tau. \tag{3.3}$$

It is noteworthy that the empirical overstress function Φ may be determined basing on available experimental results performed under dynamic loading.

4. Kinematics of finite deformation and fundamental definitions

Let $\{X^A\}$ and $\{x^a\}$ denote coordinate systems on $\mathcal{B}$ and $\mathcal{S}$ respectively. Then we refer to $\mathcal{B} \subset \mathbb{R}^3$ as the reference configuration of a continuum body with particles $X \in \mathcal{B}$ and to $\mathcal{S} = \phi(\mathcal{B})$ as the current configuration with points $\mathbf{x} \in \mathcal{S}$. The matrix $\mathbf{F}(\mathbf{X},t) = \partial\phi(\mathbf{X},t)/\partial\mathbf{X}$ with respect to the coordinate bases $\mathbf{E}_A(\mathbf{X})$ and $\mathbf{e}_a(\mathbf{x})$ is given by

$$F^a_A(\mathbf{X},t) = \frac{\partial\phi^a}{\partial X^A}(\mathbf{X},t), \tag{4.1}$$

where a mapping $\mathbf{x} = \phi(\mathbf{X},t)$ represents a motion of a body $\mathcal{B}$.

We consider the local multiplicative decomposition

$$\mathbf{F} = \mathbf{F}^e \cdot \mathbf{F}^p, \tag{4.2}$$

where $(\mathbf{F}^e)^{-1}$ is the deformation gradient that releases elastically the stress on the neighborhood $\phi(\mathcal{N}(\mathbf{X}))$ in the current configuration.

Let us define the total and elastic Finger deformation tensors

$$\mathbf{b} = \mathbf{F} \cdot \mathbf{F}^T, \qquad \mathbf{b}^e = \mathbf{F}^e \cdot \mathbf{F}^{e^T}, \tag{4.3}$$

respectively, and the Eulerian strain tensors as follows:

$$\mathbf{e} = \frac{1}{2}\left(\mathbf{g} - \mathbf{b}^{-1}\right), \qquad \mathbf{e}^e = \frac{1}{2}\left(\mathbf{g} - \mathbf{b}^{e^{-1}}\right), \tag{4.4}$$

where $\mathbf{g}$ denotes the metric tensor in the current configuration.

By definition[1)]

$$\mathbf{e}^p = \mathbf{e} - \mathbf{e}^e = \frac{1}{2}\left(\mathbf{b}^{e^{-1}} - \mathbf{b}^{-1}\right) \tag{4.5}$$

we introduce the plastic Eulerian strain tensor.

To define objective rates for vectors and tensors we use the Lie derivative[2)]. Let us define the Lie derivative of a spatial tensor field $\mathbf{t}$ with respect to the velocity field $\boldsymbol{\upsilon}$ as

$$\mathrm{L}_{\boldsymbol{\upsilon}}\mathbf{t} = \phi_* \frac{\partial}{\partial t}(\phi^* \mathbf{t}), \tag{4.6}$$

where ϕ^* and ϕ_* denote the pull-back and push-forward operations, respectively.

The rate of deformation is defined as follows:

$$\mathbf{d}^\flat = \mathrm{L}_{\boldsymbol{\upsilon}}\mathbf{e}^\flat = \frac{1}{2}\mathrm{L}_{\boldsymbol{\upsilon}}\mathbf{g} = \frac{1}{2}\left(g_{ac}\upsilon^c \mid_b + g_{cb}\upsilon^c \mid_a\right)\mathbf{e}^a \otimes \mathbf{e}^b, \tag{4.7}$$

where the symbol $\flat$ denotes the index lowering operator and $\otimes$ the tensor product,

$$\upsilon^a \mid_b = \frac{\partial \upsilon^a}{\partial x^b} + \gamma^a_{bc}\upsilon^c, \tag{4.8}$$

and γ^a_{bc} denotes the Christoffel symbol for the general coordinate systems $\{x^a\}$. The components of the spin $\boldsymbol{\omega}$ are given by

$$\omega_{ab} = \frac{1}{2}\left(g_{ac}\upsilon^c \mid_b - g_{cb}\upsilon^c \mid_a\right) = \frac{1}{2}\left(\frac{\partial \upsilon_a}{\partial x^b} - \frac{\partial \upsilon_b}{\partial x^a}\right). \tag{4.9}$$

Similarly

$$\mathbf{d}^{e^\flat} = \mathrm{L}_{\boldsymbol{\upsilon}}\mathbf{e}^{e^\flat}, \qquad \mathbf{d}^{p^\flat} = \mathrm{L}_{\boldsymbol{\upsilon}}\mathbf{e}^{p^\flat}, \tag{4.10}$$

[1)] For precise definition of the finite elasto-plastic deformation see PERZYNA [38].

[2)] The algebraic and dynamic interpretations of the Lie derivative have been presented by ABRAHAM *et al.* [2], ABRAHAM and MARSDEN [1], cf. also MARSDEN and HUGHES [22].

and

$$\mathbf{d} = \mathbf{d}^e + \mathbf{d}^p. \tag{4.11}$$

Let $\boldsymbol{\tau}$ denote the Kirchhoff stress tensor related to the Cauchy stress tensor $\boldsymbol{\sigma}$ by

$$\boldsymbol{\tau} = J\boldsymbol{\sigma} = \frac{\rho_{\mathrm{Ref}}}{\rho}\boldsymbol{\sigma}, \tag{4.12}$$

where the Jacobian J is the determinant of the linear transformation

$$\mathbf{F}(\mathbf{X}, t) = (\partial/\partial X)\phi(\mathbf{X}, t),$$

$\rho_{\mathrm{Ref}}(\mathbf{X})$ and $\rho(\mathbf{x}, t)$ denote the mass density in the reference and current configuration, respectively.

The Lie derivative of the Kirchhoff stress tensor $\boldsymbol{\tau} \in \mathbf{T}^2(\mathcal{S})$ (elements of $\mathbf{T}^2(\mathcal{S})$ are called tensors on $\mathcal{S}$, contravariant of order 2) gives

$$\begin{aligned} \mathrm{L}_{\boldsymbol{\upsilon}}\boldsymbol{\tau} = \phi_* \frac{\partial}{\partial t}(\phi^*\boldsymbol{\tau}) &= \left\{ \mathbf{F} \cdot \frac{\partial}{\partial t}\left[\mathbf{F}^{-1} \cdot (\boldsymbol{\tau} \circ \phi) \cdot \mathbf{F}^{-1^T} \right] \cdot \mathbf{F}^T \right\} \circ \phi^{-1} \\ &= \dot{\boldsymbol{\tau}} - (\mathbf{d} + \boldsymbol{\omega}) \cdot \boldsymbol{\tau} - \boldsymbol{\tau} \cdot (\mathbf{d} + \boldsymbol{\omega})^T, \end{aligned} \tag{4.13}$$

where $\circ$ denotes the composition of mappings.

5. Thermo-elasto-viscoplasticity constitutive model

5.1. Constitutive postulate

Let us assume that: (i) conservation of mass, (ii) balance of momentum, (iii) balance of moment of momentum, (iv) balance of energy, (v) entropy production inequality, hold.

We introduce the four fundamental postulates:

(i) Existence of the free energy function. It is assumed that the free energy function is given by

$$\psi = \widehat{\psi}(\mathbf{e}, \mathbf{F}, \vartheta; \boldsymbol{\mu}), \tag{5.1}$$

where ϑ is temperature and $\boldsymbol{\mu}$ denotes a set of the internal state variables. To extend the domain of the description of the material properties and particularly, to take into consideration different dissipation effects, we have to introduce the internal state variables represented by the vector $\boldsymbol{\mu}$.

(ii) Axiom of objectivity (spatial covariance). The constitutive structure should be invariant with respect to any diffeomorphism (any motion) $\zeta : \mathcal{S} \to \mathcal{S}$.

(iii) The axiom of the entropy production. For any regular motion of a body $\mathcal{B}$, the constitutive functions are assumed to satisfy the reduced dissipation inequality

$$\frac{1}{\rho_{\mathrm{Ref}}}\boldsymbol{\tau} : \mathbf{d} - (\eta\dot{\vartheta} + \dot{\psi}) - \frac{1}{\rho\vartheta}\mathbf{q} \cdot \mathrm{grad}\vartheta \geq 0, \tag{5.2}$$

where η is the specific (per unit mass) entropy, and $\mathbf{q}$ denotes the heat flow vector field.

(iv) The evolution equation for the internal state variable vector $\boldsymbol{\mu}$ is assumed in the form as follows:

$$\mathrm{L}_{\boldsymbol{\upsilon}}\boldsymbol{\mu} = \widehat{\mathbf{m}}(\mathbf{e}, \mathbf{F}, \vartheta, \boldsymbol{\mu}), \tag{5.3}$$

where the evolution function $\widehat{\mathbf{m}}$ has to be determined based on careful physical interpretation of a set of the internal state variables and the analysis of available experimental observations.

The determination of the evolution function $\widehat{\mathbf{m}}$ (in practice, a finite set of the evolution functions) appears to be the main problem of the modern constitutive modeling.

5.2. Fundamental assumptions

Experimental observation results and analysis of physical foundations (cf. Secs. 2 and 3) suggest that the fundamental mechanism of visciplastic flow is most important for proper description of *fcc*, *bcc* and *hcp* nanocrystalline metals. We intend to describe this main mechanism of viscoplastic flow by introducing the equivalent viscoplastic deformation ϵ^P as the internal state variable.

Strain rate sensitivity of these materials is very mech influenced by micro(nano)shear banding, which occurs very early during both the quasi-static and high-rate deformation processes.

Since the process of macroshear localization in these materials for all smaller grain sizes ($d < 300$ nm) develops almost immediately after the onset of viscoplastic deformation, the mechanisms of anisotropic intrinsic micro(nano)damage play a very important role. To describe the effects of anisotropic intrinsic micro(nano)damage, we intend to introduce the tensorial micro(nano)damage internal state variable $\boldsymbol{\xi}$.

Based on experimental observations, we can suggest that the intrinsic micro(nano)damage process in nanocrystalline metals depends very much on the strain-rate effects and has very anisotropic nature.

Experimental observation results presented by Shockey *et al.* [48] have shown that coalescence mechanism can be treated as nucleation and growth

process on a smaller scale. This conjecture simplifies very much the description of the intrinsic micro(nano)damage process by taking account only of the nucleation and growth mechanisms.

Recent investigations of plastic behaviour of nanocrystalline metals suggest that the anisotropy induced by finite plastic deformation plays also a fundamental role. This induced anisotropy is mainly caused by the residual stresses which are generated by the heterogeneous nature of plastic deformation in nanocrystalline metals. To describe these effects of plastic strain-induced anisotropy, the residual stress tensor (the back stress tensor) $\boldsymbol{\alpha}$ has to be introduced to the constitutive structure as the internal state variable. The aim of this is to take into account the kinematic hardening phenomenon, which can be treated as the first approximation of the description of plastic deformation-induced anisotropy.

The mechanism of rotation of neighboring nanograins during intense viscoplastic deformation process observed experimentally has to be described by taking account of finite viscoplastic deformation and the viscoplastic spin.

The dynamic grain growth process observed experimentally is easy to take into account by introducing the mean grain diameter d as the internal state variable.

For our practical purposes it is sufficient to assume that the internal state vector $\boldsymbol{\mu}$ has the form

$$\boldsymbol{\mu} = (\epsilon^p, \boldsymbol{\xi}, \boldsymbol{\alpha}, d), \tag{5.4}$$

where ϵ^p is the equivalent viscoplastic deformation, i.e.

$$\epsilon^p = \int_0^t \left(\frac{2}{3} \mathbf{d}^p : \mathbf{d}^p \right)^{1/2} dt, \tag{5.5}$$

$\boldsymbol{\xi}$ denotes the microdamage second-order tensor, with the physical interpretation that $(\boldsymbol{\xi} : \boldsymbol{\xi})^{1/2} = \xi$ defines the volume fraction porosity and takes account for microdamaged effects, $\boldsymbol{\alpha}$ denotes the residual stress (the back stress) and aims at the description of the kinematic hardening effects, d defines the mean grain diameter and is introduced as the internal state variable to describe the dynamic grain growth during deformation process.

Let us introduce the plastic potential function $f = f(\widetilde{J}_1, \widetilde{J}_2, \vartheta, \boldsymbol{\mu})$, where $\widetilde{J}_1$, $\widetilde{J}_2$ denote the first two invariants of the stress tensor $\widetilde{\boldsymbol{\tau}} = \boldsymbol{\tau} - \boldsymbol{\alpha}$.

Let us postulate the evolution equations as follows:

$$\mathbf{d}^p = \Lambda \mathbf{P}, \quad \boldsymbol{\omega}^p = \Lambda \boldsymbol{\Omega}, \quad \mathrm{L}_{\upsilon} \boldsymbol{\xi} = \boldsymbol{\Xi}, \quad \mathrm{L}_{\upsilon} \boldsymbol{\alpha} = \mathbf{A}, \quad \dot{d} = \mathcal{D}, \tag{5.6}$$

where for elasto-viscoplastic model of a material we assume (cf. Perzyna [28–30, 38, 42])

$$\Lambda = \frac{1}{T_m} \left\langle \Phi \left(\frac{f}{\kappa} - 1 \right) \right\rangle, \tag{5.7}$$

T_m denotes the relaxation time for mechanical disturbances, the isotropic work-hardening-softening function κ is

$$\kappa = \widehat{\kappa}(\epsilon^p,\ \vartheta,\ \boldsymbol{\xi},\ d), \tag{5.8}$$

Φ is the empirical overstress function, the bracket $\langle\cdot\rangle$ defines the ramp function,

$$\mathbf{P} = \left.\frac{\partial f}{\partial \boldsymbol{\tau}}\right|_{\boldsymbol{\xi}=\text{const}} \left(\left|\left|\frac{\partial f}{\partial \boldsymbol{\tau}}\right|\right|\right)^{-1}, \tag{5.9}$$

$\boldsymbol{\Omega}$, $\boldsymbol{\Xi}$, $\mathbf{A}$ and $\mathcal{D}$ denote the evolution functions which have to be determined.

5.3. Microshear banding effects

To describe the microshear banding effects let us assume that the relaxation time T_m depends on the active microshear bands fraction f_{ms} and on the rate of equivalent viscoplastic deformation $\dot{\epsilon}^P$ (cf. Pęcherski [46], Nowak, Perzyna and Pęcherski [27] and Perzyna [43]), i.e.

$$T_m = T_m\left(f_{ms}, \dot{\epsilon}^P\right). \tag{5.10}$$

Additionally, we introduce the simplification as follows:

$$T_m = T_m^0 \phi_1\left(f_{ms}\right) \phi_2\left(\dot{\epsilon}^P\right), \tag{5.11}$$

where T_m^0 is material function of the mean grain diameter d.

For example, for nanocrystalline iron we can postulate

$$\phi_1\left(f_{ms}\right) = \left[1 - f_{ms}\left(\epsilon^P\right)\right] = \left[1 - f_{ms}^0 \frac{1}{1+\exp\left(a - b\epsilon^P\right)}\right], \tag{5.12}$$

and

$$\phi_2\left(\dot{\epsilon}^P\right) = \left(\frac{\dot{\epsilon}^P}{\dot{\epsilon}_s^P} - 1\right)^{1/p}, \tag{5.13}$$

where f_{ms}^0, a, b, p and $\dot{\epsilon}_s^P$ are material function of d.

Finally we have

$$T_m = T_m^0 \left[1 - f_{ms}^0 \frac{1}{1+\exp\left(a - b\epsilon^P\right)}\right] \left(\frac{\dot{\epsilon}^P}{\dot{\epsilon}_s^P} - 1\right)^{1/p}. \tag{5.14}$$

5.4. Constitutive assumption for the viscoplastic spin

Based on experimental observations that the nanosized grains rotate during plastic deformation (cf. Subsec. 2.8), we suggest that in the proper description of nanocrystalline metals the viscoplastic spin may play a very important role.

Let us postulate that $\mathbf{\Omega}$ has the form[3)] (cf. DAFALIAS [6] and LORET [21])

$$\mathbf{\Omega} = \eta^*(\boldsymbol{\alpha} \cdot \mathbf{P} - \mathbf{P} \cdot \boldsymbol{\alpha}), \tag{5.15}$$

where η^* denotes the scalar-valued function of the invariants of the tensors $\boldsymbol{\alpha}$, $\boldsymbol{\xi}$ and $\mathbf{P}$, and may depend on temperature ϑ and the mean grain diameter d.

5.5. Anisotropic intrinsic microdamage mechanisms

To take into consideration the observed time-dependent effects, it is advantageous to use the proposition of the description of the intrinsic microdamage process presented by PERZYNA [34, 35], DUSZEK–PERZYNA and PERZYNA [10], and DORNOWSKI and PERZYNA [8].

Let us assume that the intrinsic microdamage process consists of the nucleation and growth mechanisms.

Based on the heuristic suggestions and taking into account the influence of the stress triaxiality and anisotropic effects on the nucleation and growth mechanisms, we assume the evolution equation for the microdamage tensor $\boldsymbol{\xi}$ as follows (cf. PERZYNA [43]):

$$\mathrm{L}_{\boldsymbol{\upsilon}}\boldsymbol{\xi} = \frac{\partial h^*}{\partial \boldsymbol{\tau}} \frac{1}{T_m} \left\langle \Phi \left[\frac{\widetilde{I}_n}{\tau_n(\boldsymbol{\xi}, \boldsymbol{\alpha}, \vartheta, \epsilon^p, d)} - 1 \right] \right\rangle + \frac{\partial g^*}{\partial \boldsymbol{\tau}} \frac{1}{T_m} \left\langle \Phi \left[\frac{\widetilde{I}_g}{\tau_{eq}(\boldsymbol{\xi}, \boldsymbol{\alpha}, \vartheta, \epsilon^p, d)} - 1 \right] \right\rangle . \tag{5.16}$$

The tensorial function $\partial h^*/\partial \boldsymbol{\tau}$ describes the mutual microcrack interaction for nucleation mechanism, while the tensorial function $\partial g^*/\partial \boldsymbol{\tau}$ represents the mutual microcrack interaction for growth process, τ_n and τ_{eq} denote the threshold stresses for microcrack nucleation and growth, respectively.

$$\widetilde{I}_n = a_1 \widetilde{J}_1 + a_2 \sqrt{\widetilde{J}_2} + a_3 \left(\widetilde{J}_3 \right)^{1/3} \tag{5.17}$$

[3)] For a thorough discussion of a concept of the plastic spin and its constitutive description in phenomenological theories for macroscopic large plastic deformations, please consult the critical review paper by VAN DER GIESSEN [50].

defines the stress intensity invariant for nucleation, a_i $(i = 1, 2, 3)$ are the material coefficients which can depend on d, $\widetilde{J}_2'$ and $\widetilde{J}_3'$ are the second and third invariants of the stress deviator $\widetilde{\boldsymbol{\tau}}' = (\boldsymbol{\tau} - \boldsymbol{\alpha})'$,

$$\widetilde{I}_g = b_1 \widetilde{J}_1 + b_2 \sqrt{\widetilde{J}_2'} + b_3 \left(\widetilde{J}_3'\right)^{1/3}, \tag{5.18}$$

defines the stress intensity invariant for growth and b_i $(i = 1, 2, 3)$ are the material coefficient which can depend on d. This determines the evolution function $\boldsymbol{\Xi}$.

In the evolution Eq. (5.16) the functions

$$h = \widehat{h}\left(\boldsymbol{\tau}, \vartheta, \epsilon^P, \boldsymbol{\xi}, \boldsymbol{\alpha}, d\right), \tag{5.19}$$

$$g = \widehat{g}\left(\boldsymbol{\tau}, \vartheta, \epsilon^P, \boldsymbol{\xi}, \boldsymbol{\alpha}, d\right), \tag{5.20}$$

play the fundamental role, and have to be determined based on available experimental observation data. We also introduced the denotations as follows

$$\frac{\partial h^*}{\partial \boldsymbol{\tau}} = \frac{\partial \widehat{h}}{\partial \boldsymbol{\tau}} \left(\left|\left| \frac{\partial \widehat{h}}{\partial \boldsymbol{\tau}} \right|\right| \right)^{-1}, \qquad \frac{\partial g^*}{\partial \boldsymbol{\tau}} = \frac{\partial \widehat{g}}{\partial \boldsymbol{\tau}} \left(\left|\left| \frac{\partial \widehat{g}}{\partial \boldsymbol{\tau}} \right|\right| \right)^{-1}. \tag{5.21}$$

The threshold stresses τ_n and τ_{eq} for microcrack nucleation and growth, respectively, can be assumed as the material functions in the form

$$\tau_n = \tau_n\left(\boldsymbol{\xi}, \boldsymbol{\alpha}, \vartheta, \epsilon^P, d\right), \qquad \tau_{eq} = \tau_{eq}\left(\boldsymbol{\xi}, \boldsymbol{\alpha}, \vartheta, \epsilon^P, d\right). \tag{5.22}$$

5.6. Kinematic hardening

To determine the evolution function $\mathbf{A}$ we shall follow some results obtained by Duszek and Perzyna [9]. The kinematic hardening evolution law takes the form

$$\mathrm{L}_{\upsilon}\boldsymbol{\alpha} = \frac{1}{T_m} \left\langle \Phi\left(\frac{f}{\kappa} - 1\right) \right\rangle \left[r_1 \mathbf{P} + r_2 \frac{\mathbf{P} : \mathbf{Q}}{\widetilde{\boldsymbol{\tau}} : \mathbf{Q} + r_3 \boldsymbol{\xi} : \mathbf{Q}} (\widetilde{\boldsymbol{\tau}} + r_3 \boldsymbol{\xi}) \right], \tag{5.23}$$

where r_1, r_2 and r_3 are the grain diameter-dependent material coefficients and

$$\mathbf{Q} = \left[\frac{\partial f}{\partial \boldsymbol{\tau}} + \left(\frac{\partial f}{\partial \boldsymbol{\xi}} - \frac{\partial \kappa}{\partial \boldsymbol{\xi}} \right) : \frac{\partial \boldsymbol{\xi}}{\partial \boldsymbol{\tau}} \right] \left|\left| \frac{\partial f}{\partial \boldsymbol{\tau}} + \left(\frac{\partial f}{\partial \boldsymbol{\xi}} - \frac{\partial \kappa}{\partial \boldsymbol{\xi}} \right) : \frac{\partial \boldsymbol{\xi}}{\partial \boldsymbol{\tau}} \right|\right|^{-1}. \tag{5.24}$$

The kinetic law (5.23) represents the linear combination of the Prager and Ziegler kinematic hardening rules and additionally depends linearly on the microdamage tensor $\boldsymbol{\xi}$.

5.7. Description of dynamic grain growth

Based on the heuristic suggestion and taking into consideration the conclusion from the experimental observation and the physical foundations that the dynamic grain growth is the rate-dependent mechanism, we can postulate

$$\dot{d} = \frac{\widehat{\mathcal{G}}(\vartheta, \boldsymbol{\mu})}{T_m} \left\langle \Phi \left[\frac{\widetilde{I}_d}{\tau_d(\vartheta, \boldsymbol{\mu})} - 1 \right] \right\rangle, \tag{5.25}$$

where $\mathcal{G} = \widehat{\mathcal{G}}(\vartheta, \boldsymbol{\mu})$ is the material function, and

$$\widetilde{I}_d = c_1 \widetilde{J}_1 + c_2 \sqrt{\widetilde{J}_2'} + c_3 \left(\widetilde{J}_3' \right)^{1/3} \tag{5.26}$$

represents the stress intensity invariant for grain growth, c_i $(i = 1, 2, 3)$ are the material coefficients which may depend on d, and

$$\tau_d = \tau_d(\vartheta, \boldsymbol{\mu}) \tag{5.27}$$

denotes the threshold stress for dynamic grain growth mechanism.

It is noteworthy that evolution equation (5.25) is dependent on the stress triaxility.

5.8. Thermodynamic restrictions and rate type constitutive relations

Suppose the axiom of the entropy production holds. Then the constitutive assumption (5.1) and the evolution equations (5.6) lead to the results as follows:

$$\boldsymbol{\tau} = \rho_{Ref} \frac{\partial \widehat{\psi}}{\partial \mathbf{e}}, \qquad \eta = -\frac{\partial \widehat{\psi}}{\partial \vartheta}, \qquad -\frac{\partial \widehat{\psi}}{\partial \boldsymbol{\mu}} \cdot \mathrm{L}_{\boldsymbol{\upsilon}} \boldsymbol{\mu} - \frac{1}{\rho \vartheta} \mathbf{q} \cdot \mathrm{grad} \vartheta \geq 0. \tag{5.28}$$

The rate of internal dissipation is determined by

$$\begin{aligned} \vartheta \widehat{i} &= -\frac{\partial \widehat{\psi}}{\partial \boldsymbol{\mu}} \cdot \mathrm{L}_{\boldsymbol{\upsilon}} \boldsymbol{\mu} \\ &= -\left[\sqrt{\frac{2}{3}} \frac{\partial \widehat{\psi}}{\partial \epsilon^P} + \frac{\partial \widehat{\psi}}{\partial \boldsymbol{\alpha}} : \left(r_1 \mathbf{P} + r_2 \frac{\mathbf{P} : \mathbf{Q}}{\widetilde{\boldsymbol{\tau}} : \mathbf{Q} + r_3 \boldsymbol{\xi} : \mathbf{Q}} (\widetilde{\boldsymbol{\tau}} + r_3 \boldsymbol{\xi}) \right) \right] \Lambda \\ &\quad - \frac{\partial \widehat{\psi}}{\partial \boldsymbol{\xi}} : \boldsymbol{\Xi} - \frac{\partial \widehat{\psi}}{\partial d} \mathcal{D}. \end{aligned} \tag{5.29}$$

Operating on the stress relation $(5.28)_1$ with the Lie derivative and keeping the internal state vector constant, we obtain

$$\mathrm{L}_{\boldsymbol{\upsilon}} \boldsymbol{\tau} = \mathcal{L}^e : \mathbf{d} - \mathcal{L}^{th} \dot{\vartheta} - [(\mathcal{L}^e + \mathbf{g}\boldsymbol{\tau} + \boldsymbol{\tau}\mathbf{g} + \mathcal{W}) : \mathbf{P}] \frac{1}{T_m} \left\langle \Phi \left(\frac{f}{\kappa} - 1 \right) \right\rangle, \tag{5.30}$$

where

$$\mathcal{L}^e = \rho_{\mathrm{Ref}} \frac{\partial^2 \widehat{\psi}}{\partial \mathbf{e}^2}, \qquad \mathcal{L}^{th} = -\rho_{\mathrm{Ref}} \frac{\partial^2 \widehat{\psi}}{\partial \mathbf{e} \partial \vartheta}, \tag{5.31}$$

$$\mathcal{W} = \eta^* [(\mathbf{g}\boldsymbol{\tau} - \boldsymbol{\tau}\mathbf{g}) : (\boldsymbol{\alpha}\mathbf{g} - \mathbf{g}\boldsymbol{\alpha})].$$

Substituting $\dot{\psi}$ into the energy balance equation and taking into account the results $(5.28)_3$ and (5.29), we obtain

$$\rho \vartheta \dot{\eta} = -\mathrm{div}\mathbf{q} + \rho \vartheta \widehat{i}. \tag{5.32}$$

Operating on the entropy relation $(5.28)_2$ with the Lie derivative and substituting the result into (5.32), we obtain

$$\rho c_p \dot{\vartheta} = -\mathrm{div}\mathbf{q} + \vartheta \frac{\rho}{\rho_{\mathrm{Ref}}} \frac{\partial \boldsymbol{\tau}}{\partial \vartheta} : \mathbf{d} + \rho \chi^* \boldsymbol{\tau} : \mathbf{d}^p + \rho \chi^{**} \mathbf{K} : \mathrm{L}_{\boldsymbol{\upsilon}} \boldsymbol{\xi} + \rho \chi^{***} \dot{d}, \tag{5.33}$$

where the specific heat $c_p = -\vartheta \dfrac{\partial^2 \widehat{\psi}}{\partial \vartheta^2}$ and we introduce the denotations

$$\chi^{**} \mathbf{K} = -\left(\frac{\partial \widehat{\psi}}{\partial \boldsymbol{\xi}} - \vartheta \frac{\partial^2 \widehat{\psi}}{\partial \vartheta \partial \boldsymbol{\xi}} \right), \qquad \chi^{***} = -\left(\frac{\partial \widehat{\psi}}{\partial d} - \vartheta \frac{\partial^2 \widehat{\psi}}{\partial \vartheta \partial d} \right) \tag{5.34}$$

and χ^*, χ^{**} and χ^{***} are the irreversibility coefficients.

5.9. Length-scale sensitivity of the constitutive model

The constitutive equations for a thermo-elastic-viscoplastic model introduce implicitly a length-scale parameter into the dynamic initial-boundary value problem, i.e.

$$l = \beta c T_m = \beta(d) c T_m^0 \phi_1(f_{ms}) \phi_2(\dot{\epsilon}^P), \tag{5.35}$$

where c denotes the velocity of the propagation of the elastic waves in the problem under consideration and the proportionality factor β depends on the particular initial-boundary value problem and may also depend on the nanoscopic properties of the material as well as on the mean grain diameter.

As an example for nanocrystalline iron we have

$$l = \beta(d) c T_m^0(d) \left\{ 1 - f_{ms}^0(d) \frac{1}{1 + \exp\left[a(d) - b(d)\epsilon^P\right]} \right\} \left[\frac{\dot{\epsilon}^P}{\dot{\epsilon}_s^P(d)} - 1 \right]^{1/p}. \tag{5.36}$$

It is noteworthy to stress that the length-scale sensitivity of the constitutive structure is of great importance for proper description of particular initial-boundary value problems by using the numerical methods.

To expect the proper description we have to postulate $l < d$. This assumption can be treated as the important condition which has to be satisfied in the identification procedure.

For particular one-dimensional case for nanocrystalline iron we have

$$l=2\frac{\sigma_0+kd^{-n}}{\sqrt{\rho E}}T_m^0(d)\left\{1-f_{ms}^0(d)\frac{1}{1+\exp\left[a(d)-b(d)\epsilon^P\right]}\right\}\left[\frac{\dot{\epsilon}^P}{\dot{\epsilon}_s^P(d)}-1\right]^{1/p}. \tag{5.37}$$

6. Fracture criterion based on the evolution of microdamage

We base the fracture criterion on the evolution of the microdamage tensor $\boldsymbol{\xi}$.

Let us assume that for $(\boldsymbol{\xi} : \boldsymbol{\xi})^{1/2} = \xi^F$ catastrophe takes place (cf. Perzyna [33]), that is

$$\kappa = \widehat{\kappa}(\epsilon^p, \vartheta, \boldsymbol{\xi}, d)|_{(\boldsymbol{\xi}:\boldsymbol{\xi})^{1/2}=\xi^F} = 0. \tag{6.1}$$

It means that for $(\boldsymbol{\xi} : \boldsymbol{\xi})^{1/2} = \xi^F$ the material loses its carrying capacity. The condition (6.1) describes the main feature observed experimentally that the load tends to zero at the fracture point.

In is noteworthy that the isotropic hardening-softening material function $\widehat{\kappa}$ proposed in Eq. (5.8) should satisfy the fracture criterion (6.1).

From the condition (6.1) we may have the critical value of the equivalent inelastic deformation at the fracture point

$$\epsilon_F^P = \widehat{\mathcal{F}}(\vartheta, \xi^F, d). \tag{6.2}$$

7. Epilogue

The thermodynamical theory of elasto-viscoplasticity of nanocrystalline metals has been developed within the framework of the rate-type covariance constitutive structure, with a finite set of the internal state variables. The crucial idea in the present theory is the very efficient physical interpretation of the assumed internal state variables (as the equivalent inelastic deformation ϵ^P, the microdamage tensor $\boldsymbol{\xi}$, the residual stress tensor (the back-stress tensor) $\boldsymbol{\alpha}$ and the mean grain diameter d) and the proposition of the evolution equations for them.

We may say that this developed theory is the realization of our previous hope presented in the papers by Perzyna [43, 44]. We have to admit that the developed theory is very general and very complex. However, in practical application of it and particularly, in the solution of the initial-boundary value problems in modern manufactoring processes, we may use its special version when only some of the internal state variables will play a fundamental role.

It is noteworthy that the thermodynamical theory of elasto-viscoplasticity of nanocrystalline metals developed in this paper has been inspired by the brilliant

new developments in experimental investigations, as well as several mechanisms based and physically motivated models published in the literature, especially during the last ten years.

It is important to stress that very fundamental feature of the developed theory is its length-scale sensitivity. This has particularly a great effect for the solution of the initial-boundary value problems by using the numerical methods.

Acknowledgment

The support of the Polish Ministry of Higher Education and Science, under grants N N519 419435 and 0364/B/T02/2008/35, is kindly acknowledged.

References

1. R. Abraham, J. E. Marsden, *Foundations of Mechanics*, Second Edition, Addison-Wesley, Reading Mass., 1988.
2. R. Abraham, J. E. Marsden, T. Ratiu, *Manifolds, Tensor Analysis and Applications*, Springer, Berlin 1988.
3. R. J. Asaro, S. Suresh, *Mechanistic models for the activation volume and rate sensitivity in metals with nanocrystalline grains and nano-scale twins*, Acta Materialia, **53**, 3369–3382, 2005.
4. S. Cheng, E. Ma, Y. M. Wang, L. Y. Kecskes, K. M. Youssef, C. C. Koch, U. P. Trociewitz, K. Han, *Tensile properties of in situ consolidated nanocrystalline Cu*, Acta Materialia, **53**, 1521–1533, 2005.
5. B. D. Coleman, W. Noll, *The thermodynamics of elastic materials with heat conduction and viscosity*, Arch. Rational Mech. Anal., **13**, 167–178, 1963.
6. Y.F. Dafalias, *Corotational rates for kinematic hardening at large plastic deformations*, J. Appl. Mech., **50**, 561–565, 1983.
7. M. Dao, L. Lu, R. J. Asaro, J. T. M. De Hosson, E. Ma, *Toward a quantitative understanding of mechanical behaviour of nanocrystalline metals*, Acta Materialia, **55**, 12, 4041–4065, 2007.
8. W. Dornowski, P. Perzyna, *Localization phenomena in thermo-viscoplastic flow processes under cyclic dynamic loadings*, Computer Assisted Mechanics and Engineering Sciences, **7**, 117–160, 2000.
9. M. K. Duszek–Perzyna, P. Perzyna, *On combined isotropic and kinematic hardening effects in plastic flow processes*, Int. J. Plasticity, **7**, 351–363, 1991.
10. M. K. Duszek–Perzyna, P. Perzyna, *Analysis of the influence of different effects on criteria for adiabatic shear band localization in inelastic solids*, [in:] Material Instabilities: Theory and Applications, ASME Congress, Chicago, 9–11 November 1994, R.C. Batra and H.M. Zbib [Eds.], AMD–Vol. 183/MD–Vol.50, ASME, New York, 1994, pp. 59–85.
11. R. Ebrahimi, G. R. Bourne, M. S. Kelly, T. E. Matthews, *Mechanical properties of nanocrystalline nickel produced by electrodeposition*, NanoStructured Materials, **11**, 343–350, 1999.

12. T. Hanlon, N. Y. Kwon, S. Suresh, *Grain size effects on the fatigue response of nanocrystalline metals*, Scripta Mater., **49**, 675–680, 2003.

13. T. Hanlon, E. D. Tabachnikowa, S. Suresh, *Fatigue behaviour of nanocrystalline metals and alloys*, Int. J. Fatigue, **27**, 1147–1158, 2005.,

14. A. Glema, T. Łodygowski, W. Sumelka, P. Perzyna, *The numerical analysis of the intrinsic anisotropic microdamage evolution in elastic-viscoplastic solids*, Int. J. Damage Mechanics, **18**, 205–231, 2009.

15. D. Jia, Y. M. Wang, K. T. Ramesh, E. Ma, Y. T. Zhu, R. Z. Valiev, *Deformation behavior and plastic instabilities of ultrafine-grain titanium*, Applied Physics Letters, **79**, 611–613, 2001.

16. S. P. Jia, K. T. Ramesh, E. Ma, *Effects of nanocrystalline and ultrafine grain sizes on constitutive behaviour and shear bands in iron*, Acta Materialia, **51**, 3495–3509, 2003.

17. S. P. Joshi, K. T. Ramesh, *Grain size dependent shear instabilities in body-centered and face-centered cubic materials*, Materials Science and Engineering A, **493**, 65–70, 2008.

18. K. Korbel, Z. Nowak, P. Perzyna, R. B. Pęcherski, *Viscoplasticity of nanometals based on Burzyński yield condition*, 35th Solid Mechanics Conference, Kraków, Poland, September 4–8, 2006.

19. K. S. Kumar, S. Suresh, M. F. Chisolm, J. A. Horton, P. Wang, *Deformation of electrodeposited nanocrystalline nickel*, Acta Materialia, **51**, 387–405, 2003.

20. R. A. Lebenson, E. M. Bringa, A. Caro, *A viscoplastic micromechanical model for the yield strength of nanocrystalline materials*, Acta Materialia, **55**, 261–271, 2007.

21. B. Loret, *On the effects of plastic rotation in the finite deformation of anisotropic elasto-plastic materials*, Mech. Mater., **2**, 287–304, 1983.

22. J. E. Marsden, T. J. R. Hughes, *Mathematical Foundations of Elasticity*, Prentice-Hall, Englewood Cliffs, New York 1983.

23. H. C. Meyers, *Dynamic Behaviour of Materials*, John Wiley, New York 1994.

24. M. A. Meyers, A. Mishra, D. J. Benson, *Mechanical properties of nanocrystalline materials*, Progress in Materials Science, **51**, 427–556, 2006.

25. M. A. Meyers, A. Mishra, D. J. Benson, *The deformation physics of nanocrystalline metals: Experiments, analysis and computations*, JOM, 41–48, 2006.

26. M. A. Meyers, C. T. Aimone, *Dynamic fracture (spalling) of metals*, Prog. Mater. Sci., **28**, 1–96, 1983.

27. Z. Nowak, P. Perzyna, R. B. Pęcherski, *Description of viscoplastic flow accounting for shear banding*, Arch. of Metallurgy and Materials, **52**, 217–222, 2007.

28. P. Perzyna, *The constitutive equations for rate sensitive plastic materials*, Quart. Appl. Math., **20**, 321–332, 1963.

29. P. Perzyna, *Fundamental problems in viscoplasticity*, Advances in Applied Mechanics, **9**, 343–377, 1966.

30. P. Perzyna, *Thermodynamic theory of viscoplasticity*, Advances in Applied Mechanics, **11**, 313–354, 1971.

31. P. Perzyna, *Coupling of dissipative mechanisms of viscoplastic flow*, Arch. Mechanics, **29**, 607–624, 1977.

32. P. Perzyna, *Modified theory of viscoplasticity. Application to advanced flow and instability phenomena*, Arch. Mechanics, **32**, 403–420, 1980.

33. P. Perzyna, *Constitutive modelling of dissipative solids for postcritical behaviour and fracture*, ASME J. Eng. Materials and Technology, **106**, 410–419, 1984.

34. P. Perzyna, *Internal state variable description of dynamic fracture of ductile solids*, Int. J. Solids Structures, **22**, 797–818, 1986.

35. P. Perzyna, *Constitutive modelling for brittle dynamic fracture in dissipative solids*, Arch. Mechanics, **38**, 725–738, 1986.

36. P. Perzyna, *Temperature and rate dependent theory of plasticity of crystalline solids*, Revue Phys. Appl., **23**, 445–459, 1988.

37. P. Perzyna, *Instability phenomena and adiabatic shear band localization in thermoplastic flow processes*, Acta Mechanica, **106**, 173–205, 1994.

38. P. Perzyna, *Interactions of elastic–viscoplastic waves and localization phenomena in solids*, IUTAM Symposium on Nonlinear Waves in Solids, August 15–20, 1993, Victoria, Canada, J.L. Wegner and F.R. Norwood [Eds.], ASME 1995, pp. 114–121.

39. P. Perzyna, *Constitutive modelling of dissipative solids for localization and fracture*, in: Localization and Fracture Phenomena in Inelastic Solids, P. Perzyna [Ed.], Springer, Wien, New York, pp. 99–242, 1998.

40. P. Perzyna, *Thermo-elasto-viscoplasticity and damage*, [in:] Handbook of Materials Behaviour Models, J. Lemaitre [Ed.], Academic Press, New York, pp. 821–834, 2001.

41. P. Perzyna, *Thermodynamical theory of inelastic single crystals*, Engineering Transactions, **50**, 107–164, 2002.

42. P. Perzyna, *The thermodynamical theory of elasto-viscoplasticity*, Engineering Transactions, **53**, 235–316, 2005.

43. P. Perzyna, *The thermodynamical theory of elasto-viscoplasticity accounting for microshear banding and induced anisotropy effects*, Mechanics, **27**, 25–42, 2008.

44. P. Perzyna, *Application of the thermodynamical theory of elasto-viscoplasticity in modern manufacturing processes*, CISM Courses and Lectures, Springer: Wien, New York, 2010 (in print).

45. P. Perzyna, G. Z. Voyiadjis, *Thermodynamic theory of elasto-viscoplasticity for induced anisotropy effects*, McMat 2005, Mechanics and Materials Conference, June 1–3, 2005, Baton Rouge, LA, USA, 2005.

46. R. B. Pęcherski, *Macroscopic effects of microshear banding in plasticity of metals*, Acta Mechanica, **131**, 203–224, 1998.

47. R. Schwaiger, B. Moser, M. Dao, N. Chollacoop, S. Suresh, *Some critical experiments on the strain-rate sensitivity of nanocrystalline nickel*, Acta Materialia, **51**, 5159–5172, 2003.

48. D. A. Shockey, L. Seaman, D. R. Curran, *The microstatistical fracture mechanics approach to dynamic fracture problem*, Int. J. Fracture, **27**, 145–157, 1985.

49. C. Truesdell, W. Noll, *The Non-Linear Field Theories of Mechanics*, [in:] Handbuch der Physik III/3, S. Flügge [Ed.], Springer-Verlag, Berlin 1965.

50. E. Van der Giessen, *Micromechanical and thermodynamic aspects of the plastic spin*, Int. J. Plasticity, **7**, 365–386, 1991.

51. Y. M. Wang, J. Y. Huang, T. Jiao, Y. T. Zhu, A. V. Hamza, *Abnormal strain hardening in nanostructered titanium at high strain rates and large strains*, J. Mater. Sci., **42**, 1751–1756, 2007.

52. Y. M. Wang, E. Ma, *Strain hardening, strain sensitivity, and ductility of nanostructured metals*, Materials Science and Engineering, **A375–377**, 46–52, 2004.

53. Y. M. Wang, E. Ma, *Three strategies to achieve uniform tensile deformation in nanostructured metal*, Acta Materialia, **52**, 1699–1709, 2004.

54. Y. M. Wang, E. Ma, R. Z. Valiev, Y. T. Zhu, *Tough nanostructured metals at cryogenic temperatures*, Adv. Mater., **16**, 328–331, 2004.

55. Q. Wei, T. Jiao, K. T. Ramesh, E. Ma, L. J. Keckes, L. Magness, R. J. Dowding, V. U. Kazykhanov, R. Z. Valiev, *Mechanical behavior and dynamic failure of high-strength ultrafine grained tungsen under uniaxial compression*, Acta Materialia, **54**, 77–87, 2006.

56. Q. Wei, L. Keckes, T. Jiao, K T. Hartwig, K. T. Ramesh, E. Ma, *Adiabatic shear bending in ultrafine-grained Fe processed by severe plastic deformation*, Acta Materialia, **52**, 1859–1869, 2004.

57. Q. Wei, K. T. Ramesh, E. Ma, L. J. Keckes, R. J. Dowding, V. U. Kazykhanov, R. Z. Valiev, *Plastic flow localization in bulk tungsten with ultrafine microstructure*, Applied Physics Letters, **86**, 101907(1–3), 2005.

58. Q. Wei, H. T. Zhang, B. E. Schuster, K. T. Ramesh, R. Z. Valiev, L. J. Keckes, R. J. Dowding, L. Magness, K. Cho, *Microstructure and mechanical properties of super-strong nanocrystalline tungsten processed by high-pressure torsion*, Acta Materialia, **54**, 4079–4089, 2006.

59. Y. J. Wei, L. Anand, *Grain-boundary sliding and separation in polycrystalline metals: Application to nanocrystalline fcc metals*, J. Mech. Phys. Sol., **52**, 2587–2616, 2004.

60. K. M. Youssef, R. O. Scattergood, K. L. Murty, J. A. Horton, C. C. Koch, *Ultrahigh strength and high ductility of bulk nanocrystalline copper*, Appl. Phys. Letters, **87**, 091904, 1–3, 2005.

61. X. Zhang, H. Wang, R. O. Scattergood, J. Narayan, C. C. Koch, *Mechanical properties of cyromilled nanocrystalline Zn studied by the miniaturized disk bend test*, Acta Materialia, **50**, 3527–3533, 2002.

62. Y. T. Zhu, J. Y. Huang, T. Ungar, Y. M. Wang, E. Ma, R. Z. Valiev, *Nanostructures in the Ti processed by severe plastic deformation*, J. Mater. Res., **18**, 1908–1917, 2003.

Received June 28, 2010; revised version December 8, 2010.